

Conditional Diffusion Model with Anatomical-Dose Dual Constraints for End-to-End Multi-Tumor Dose Prediction

Hui Xie^{a,b}, Haiqin Hu^c, Lijuan Ding^d, Qing Li^b, Yue Sun^{a,*}, Tao Tan^{a,*}

a. Faculty of Applied Sciences, Macao Polytechnic University, R. de Luís Gonzaga Gomes, Macao, 999078, P. R. China

b. Department of Oncology, Affiliated Hospital of Xiangnan University, No.31 Renmin West Road, Chenzhou, 423000, Hunan, P. R. China

c. Department of Oncology, Jiangxi Cancer Hospital, No. 519, Beijing East Road, Nanchang, 330029, Jiangxi, P. R. China

d. Department of Oncology, Chenzhou Third People's Hospital, No. 8, Jiankang Road, Chenzhou, 423000, Hunan, P. R. China

a
b

Abstract

Traditional manual optimization in radiotherapy planning is highly experience-dependent and time-consuming. Although deep learning offers automated solutions, existing models still face limitations in generalization across tumor types, prediction accuracy, and adherence to clinical constraints. This paper proposes a novel end-to-end multi-tumor dose prediction model—the Anatomical-Dose Dual Constraints Diffusion Model (ADDiff-Dose)—which innovatively integrates anatomical and clinical dose dual constraints into a conditional diffusion framework. We design a Lightweight 3D Variational Autoencoder (LightweightVAE3D) that compresses high-resolution CT images to 0.3% of their original size for efficient 3D data processing. In the latent space, a conditional diffusion model with a 3D U-Net backbone guides the denoising process to generate dose distributions by incorporating multimodal conditions—including target and organ-at-risk masks and beam parameters—via a multi-head attention mechanism. Furthermore, we introduce a composite loss function that not only optimizes the mean squared error of noise prediction but also, for the first time, directly "hard-codes" over 50 clinical dose-volume constraints into the optimization objectives, ensuring the clinical feasibility of the generated results. Extensive evaluations on a large-scale public dataset (2,877 cases) and three external institutional cohorts (450 cases in total) demonstrate that ADDiff-Dose significantly outperforms state-of-the-art models across nearly all key metrics. Qualitative assessments include visual comparisons and difference maps, confirming superior structural dose distributions with reduced artifacts in high-dose regions. Ablation studies further confirm that our proposed anatomical-dose dual-constraint design is core to the model's performance: removing any constraint leads to significant performance degradation, with the clinical constraint loss (L_{cond}) ablation increasing spinal cord D_{max} error by 109%, and the MSE loss (L_{mse}) ablation reducing spatial accuracy (DICE) by 8.8%. The full model enhances clinical dose compliance by 28.5% and enables uncertainty quantification through multiple stochastic inferences. This work provides a highly accurate, efficient, and generalizable automated treatment planning tool for clinical practice.

Keywords: Conditional Diffusion Model; Anatomical-Dose Dual Constraints; Dose Prediction; Multi-Tumor

2010 MSC: 00-01, 99-00

:These authors contributed equally to this work.

*Corresponding author: Tao Tan and Yue Sun
Email address: taotanjs@gmail.com and joyyuesun@gmail.com (Tao Tan^{a,*})

1. Introduction

Cancer remains a leading cause of morbidity and mortality worldwide, posing a persistent threat to human health. Among the three principal treatment modalities—surgery, chemotherapy, and radiotherapy—approximately 80% of patients with malignant tumors require radiotherapy at some stage during their disease course [1]. The efficacy of radiotherapy hinges on the precise formulation of treatment plans, which aim to maximize tumor cell eradication while sparing adjacent healthy tissues. This planning process typically demands experienced radiotherapy physicists to iteratively adjust beam parameters to generate clinically acceptable three-dimensional dose distributions, often assessed via dose-volume histograms (DVHs). However, manual planning is time-consuming and labor-intensive, usually taking several hours to days for a single case. Additionally, the final plan quality can vary significantly depending on the planner’s expertise, potentially limiting the individualization and optimality of treatment regimens [2].

In response, recent advances in deep learning have facilitated the development of data-driven models that automate dose prediction and streamline clinical workflows. Convolutional neural networks (CNNs), generative adversarial networks (GANs), and attention-based models have shown promise in learning mappings between anatomical features and dose distributions from historical datasets [3]. For example, ResNet101 has been employed to accurately predict dose for nasopharyngeal carcinoma by integrating anatomical and beam parameters with a multi-scale feature fusion mechanism [4] [5]. In the domain of lung cancer, the asymmetric A-Net architecture achieved clinically acceptable results in the 50–60 Gy range and delivered high spatial precision in mobile lesion regions [6, 7]. Traditional knowledge-based planning (KBP) approaches also remain relevant. Techniques combining kernel density estimation, k-nearest neighbors (KNN), and principal component analysis (PCA) have demonstrated the feasibility of dose modeling from limited clinical cohorts [8]. Despite encouraging progress, current methods face several limitations. First, most existing models are tailored to specific tumor types (e.g., prostate, head and neck) or limited to particular delivery techniques (e.g., IMRT, Intensity-Modulated Radiation Therapy; VMAT, Volumetric-Modulated Arc Therapy), limiting cross-domain generalization [7, 9]. Second, training data volumes remain relatively small (typically <200 patients), restricting model robustness to anatomical variability [10]. Third, prediction performance has yet to meet clinical gold standards: even advanced architectures like U-Net and 3D GAN exhibit mean absolute errors exceeding 1–3 Gy in certain regions or cases [11, 12].

In parallel, diffusion models have emerged as a powerful generative paradigm, achieving state-of-the-art performance across diverse domains such as image synthesis [13], fashion generation [14], and human motion modeling [15, 16]. Their ability to iteratively refine predictions through a learned denoising process offers unique advantages for generating complex, high-resolution outputs under multimodal constraints. However, while diffusion models have been widely adopted in computer vision, natural language processing, and other multimedia applications [17, 18, 19], their application to radiotherapy dose prediction remains relatively nascent. Only a handful of recent studies, such as DoseDiff [20] and MD-Dose [21], have begun exploring this avenue, highlighting a critical research gap in leveraging the strengths of diffusion models to handle the anatomical complexity and precision demands of radiotherapy. Existing methods still face unresolved limitations: traditional models like U-Net and GAN fail to integrate clinical dose constraints into core optimization, leading to predicted distributions that may violate safety thresholds; diffusion-based approaches such as DoseDiff [20] and MD-Dose [21] focus solely on anatomical distance or architectural design, lacking synergistic optimization of ‘anatomical structure - dose distribution’.

To address these challenges, we propose ADDiff-Dose, an end-to-end anatomical-dose dual-constrained conditional diffusion framework for multi-tumor radiotherapy dose prediction. Our model incorporates CT images, organ and target contours, prior dose maps, and beam parameters as multimodal inputs to guide a conditional generative process. By

integrating domain knowledge directly into the diffusion trajectory, ADDiff-Dose enables accurate and generalizable dose prediction for both head and neck and lung cancers under a unified architecture. Extensive experiments on multicenter datasets demonstrate its superiority in prediction accuracy, structural consistency, and cross-site adaptability, offering a promising solution for future intelligent radiotherapy planning. While pioneering studies such as DoseDiff [20] and MD-Dose [21] have demonstrated the potential of diffusion models for dose prediction, their conditioning mechanisms primarily focus on anatomical distance or Mamba-based architectures, respectively. Our work, ADDiff-Dose, distinguishes itself by introducing a comprehensive anatomical-dose dual-constraint framework. This framework explicitly encodes over 50 clinical dose-volume constraints directly into the diffusion loss function, ensuring the generated dose distributions are not only accurate but also strictly compliant with clinical protocols—a critical aspect not jointly emphasized in prior diffusion-based approaches. To validate this, we provide both quantitative metrics and qualitative visualizations comparing ADDiff-Dose with these diffusion-based baselines, demonstrating improved dose conformity and fewer violations of clinical constraints. The core innovations of this study are condensed into three key aspects:

1. **Anatomical-dose dual-constraint framework:** A novel conditioning mechanism that fuses multimodal anatomical features (tumor/OAR masks, CT intensity) with over 50 explicit clinical dose-volume constraints (e.g., spinal cord $D_{\max} \leq 45$ Gy, lung $V_{20} \leq 30\%$), breaking through the limitation of pure anatomical guidance and ensuring both spatial accuracy and clinical compliance.

2. **Efficient 3D data processing:** A Lightweight 3D-VAE specifically designed for radiotherapy scenarios, achieving 99.7% dimensional compression of high-resolution CT data while preserving key anatomical features, significantly reducing computational burden and enabling clinical deployment.

3. **Unified multi-tumor prediction architecture:** Breaking through the limitations of traditional single-tumor models, our framework enables unified intensity-modulated radiation therapy (IMRT) and volumetric modulated arc therapy (VMAT) dose prediction for both head-and-neck (H&N) and lung cancers within a single architecture. Specifically, a single model checkpoint is trained on a combined dataset (Lung + H&N), wherein tumor type (i.e., class label) is embedded as a conditional feature to mitigate inter-tumor-type interference and enhance task-specific adaptation.

2. Materials and Methods

Radiotherapy dose distribution prediction must simultaneously satisfy the dual requirements of anatomical structure fidelity and physical constraint compliance. To address the limitations of traditional unconditional diffusion models in integrating multimodal prior knowledge, this study proposes an end-to-end diffusion model based on anatomical-dose dual constraints. The model innovatively integrates multimodal inputs and prior-knowledge-guided diffusion mechanisms, enabling accurate dose prediction across tumor types within a unified architecture. The model comprises the following core components: a lightweight 3D variational autoencoder (LightweightVAE3D), a 3D UNet backbone network[22], a conditional embedding layer (ConditionalLayer), and a multi-head attention mechanism (MultiHeadAttention)[23] (Figure 1, 2 and 3). As shown in Figure 1, ADDiff-Dose operates in two stages: (1) The *LightweightVAE3D* is pre-trained to compress high-resolution CT images and dose map into a low-dimensional latent space. (2) The *conditional diffusion model* then operates entirely within this latent space. It takes the encoded latent vector z_0 and, through a progressive noising and denoising process conditioned on multimodal conditions such as clinical prior (radiotherapy dose OAR constraint table), Targets/OARs mask, Beam Information, and positional information (tumor distribution site), learns to predict the corresponding dose distribution in the latent domain. The final dose map is obtained by decoding the denoised latent vector back to the image space using the VAE decoder.

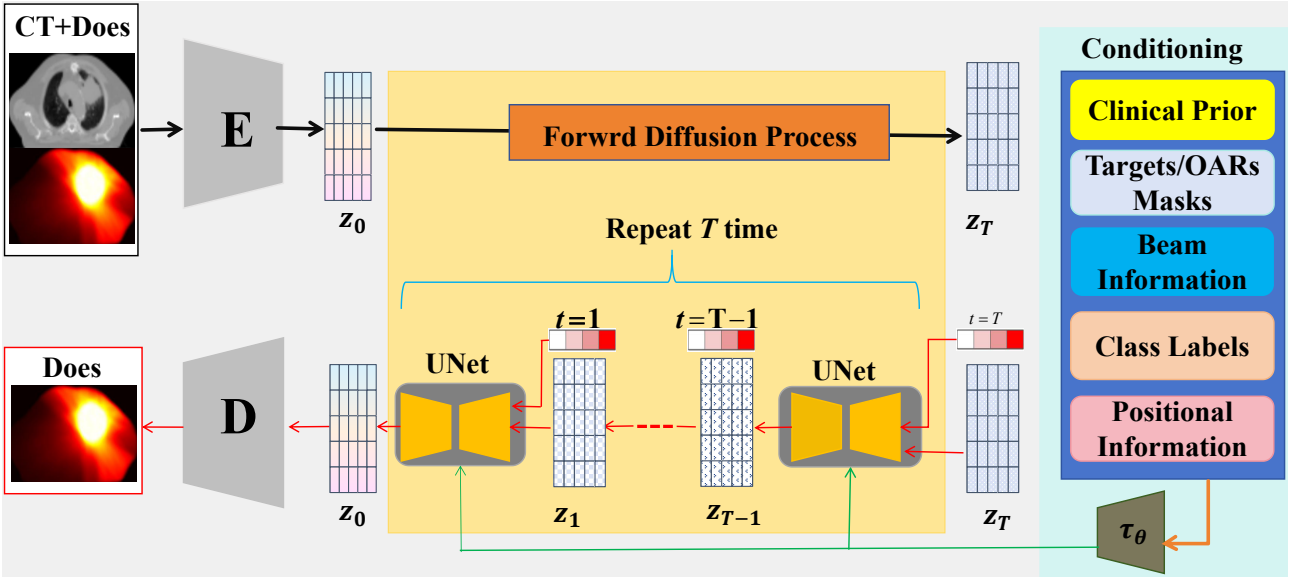


Figure 1: Overall Framework of the Anatomical-Dose Dual Constraints Conditional Diffusion Model (ADDiff-Dose). The schematic illustrates the end-to-end architecture for multi-tumor radiotherapy dose prediction. The diagram illustrates the conditional diffusion process for dose prediction. The top path shows the forward diffusion process, where the initial latent representation Z_o is progressively noised over T steps to become Z_T . The bottom path shows the reverse denoising process, where a U-Net iteratively refines Z_T back to Z_o , conditioned on multi-modal inputs including clinical priors, PTV/OAR masks, class labels, positional information, and beam parameters. The final predicted dose is obtained by decoding the denoised Z_o .

2.1. Lightweight 3D Variational Autoencoder (LightweightVAE3D)

To address the issue of dramatically increased computational complexity caused by the high resolution of the original CT images in radiotherapy dose prediction tasks, this study designed a lightweight 3D variational autoencoder (LightweightVAE3D)[24]. The model adopts a symmetric encoder-decoder architecture (Figure 2), and achieves a balance between computational efficiency and anatomical feature preservation through joint optimization of feature compression and reconstruction.

Encoder Design: The encoder employs a four-layer 3D convolutional chain (kernel size: $4 \times 4 \times 4$, stride: 2, padding: 1, activation function: StableSiLU) to perform progressive downsampling. The number of input channels increases gradually from 1 to 256 (channel expansion ratio: 1:256), enabling the model to capture hierarchical image information through multi-scale feature extraction. Ultimately, the original CT images (with a resolution of $96 \times 128 \times 144$ voxels) are compressed into a low-dimensional latent space of $6 \times 8 \times 9$ voxels, achieving a dimensionality reduction of approximately 99.7%. At the end of the encoder, fully connected layers output the Gaussian distribution parameters — mean μ and variance σ^2 — of the latent space. These parameters provide the probabilistic foundation for the subsequent diffusion process.

Decoder design: The decoder employs a symmetric 3D transposed convolution chain to gradually upsample and restore image resolution. The number of output channels decreases from 256 to 1, adapting to the normalized CT value range of 0, 1. A Sigmoid activation function is introduced to constrain the reconstructed value range, avoiding numerical overflow issues and ensuring the accuracy of anatomical structure reconstruction and clinical rationality.

Training optimization strategy: During the training phase, reparameterization techniques are introduced to enhance gradient propagation efficiency. The model jointly optimizes the adversarial loss and the reconstruction loss $L_{VAE} = \|\tilde{x} - x\|_1 + \beta D_{KL} qz|x\|pz$. Here, the Kullback-Leibler (KL) divergence D_{KL} adjusts the weight coefficient β through a dynamic annealing strategy, achieving progressive regularization of the latent space distribution. This strategy reduces

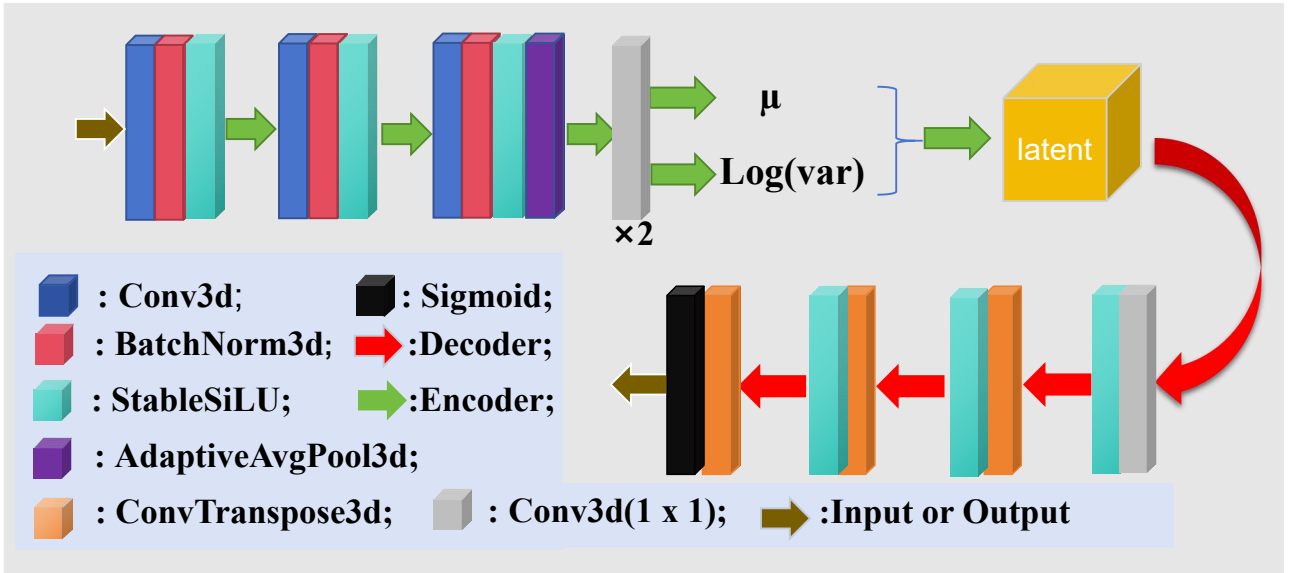


Figure 2: Architecture Diagram of the Variational Autoencoder (VAE). The upper encoding process uses layers like Conv3d, BatchNorm3d, StableSiLU, and AdaptiveAvgPool3d to generate μ and $\text{Log}(\text{var})$ for sampling the latent representation. The lower decoding process leverages ConvTranspose3d, StableSiLU, and Sigmoid layers to reconstruct output from the latent space, illustrating the full VAE workflow.

computational load while successfully preserving the morphological features of the target area and organs at risk, providing high-quality anatomical priors for subsequent diffusion models.

2.2. Conditional Diffusion Model

2.2.1. Multi-Source Conditional Feature Construction

After being processed by the VAE encoder, the 3D CT image generates a 32-dimensional latent vector z_0 , which serves as the initial input for the diffusion process. Simultaneously, multi-source conditional features are constructed as follows:

1. **Structural features:** Channel merging operations are performed on the planning target volume (PTV) mask and the organs-at-risk (OAR) masks (e.g., spinal cord, lung, brainstem) to generate a multi-channel structural tensor, which is then projected via 3D convolution to form structural conditional features.
2. **Clinical prior features:** Encode over 50 clinical dose-volume constraints (detailed in Supplementary Table 1), such as spinal cord $D_{\max} \leq 45$ Gy, lung $V_{20} \leq 30\%$, and PTV $D_{95} \geq 95\%$ of prescribed dose, into feature vectors through fully connected layers.
3. **Beam parameters:** Include beam energy (6 MV/15 MV), field angle, and number of beams as discrete features, which are converted into continuous vectors via embedding layers.
4. **Temporal features:** For discrete time steps $t \in 0, 999$, map them into high-dimensional temporal feature vectors t_{emb} through a time embedding function to capture the dynamic evolution characteristics during the diffusion process.

All conditional features are fused via the multi-head attention mechanism to form the final conditional feature C , which guides the denoising process of the diffusion model.

2.2.2. Progressive Noising and Denoising Mechanism

The noising process follows the Markov chain rule[25], using a linearly scheduled noise coefficient β_t (whose values range from 10^{-4} to 0.02), progressively injecting Gaussian noise into the latent vector:

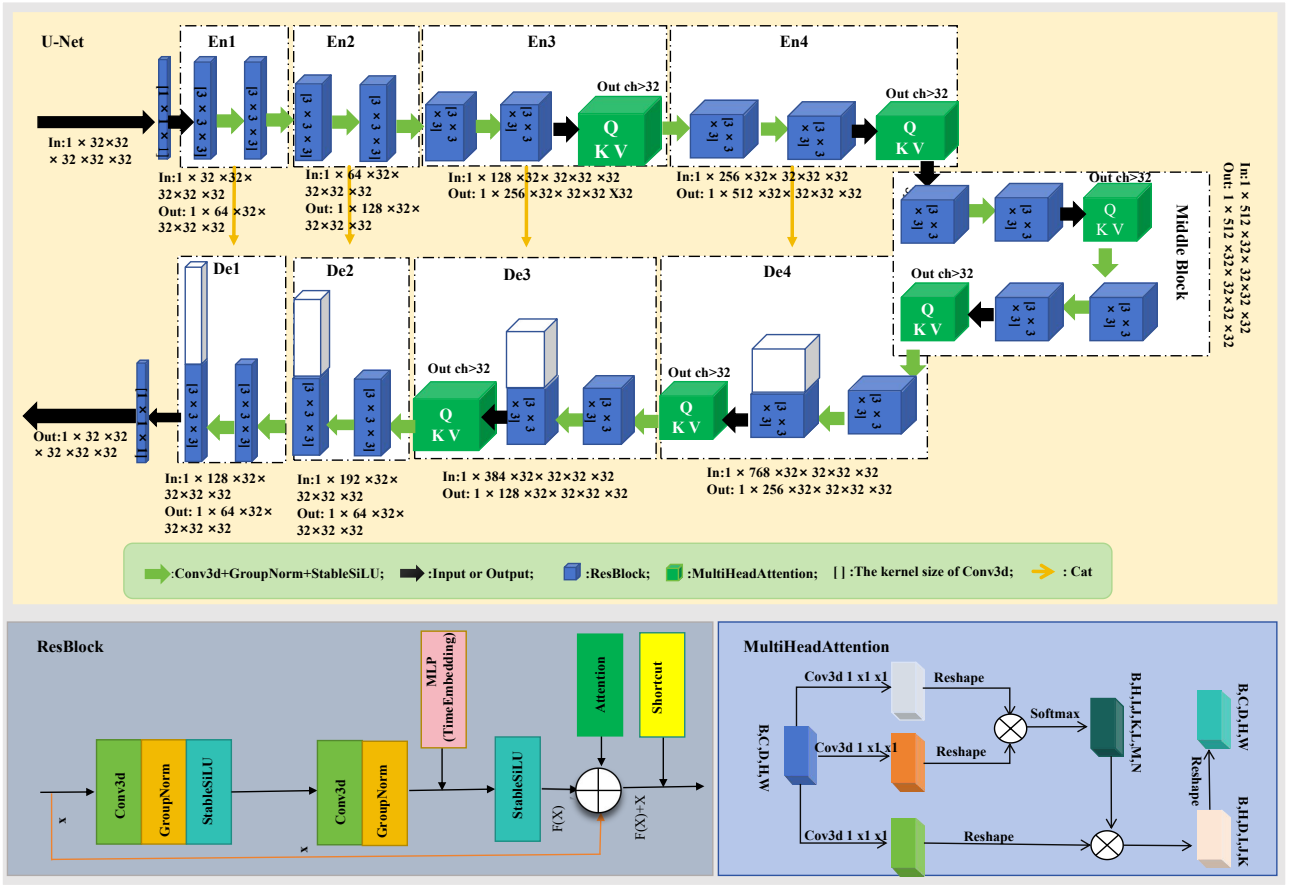


Figure 3: Architecture Diagram of the U-Net Model with Modified Attention and ResBlock Components. It shows the encoding (En1-En4) and decoding (De1-De4) paths, incorporating elements like Cascade - GroupNorm - StableSiLU, ResBlock, and MultiHeadAttention, along with detailed internal structures of ResBlock and MultiHeadAttention at the bottom.

$$z_t = \sqrt{\alpha_t} z_{t-1} + \sqrt{1 - \alpha_t} \varepsilon_{t-1}, \quad (1)$$

where $\alpha_t = 1 - \beta_t$, $\varepsilon_{t-1} \sim \mathcal{N}(0, \mathbf{I})$. Through this process, the original signal z_0 gradually degrades to Gaussian noise z_T .

The reverse denoising process is implemented by a 3D UNet (UNet3D) (Figure 3). This UNet adopts an encoder-decoder architecture, consisting of 4 layers of downsampling (channel numbers increasing from 64 to 512) and 4 layers of upsampling (channel numbers decreasing from 512 to 64), and fuses multi-scale features through skip connections. In the deeper layers, a multi-head attention mechanism is introduced.

The UNet takes the noisy vector Z_t , time embedding t_{emb} , and conditional feature C as inputs, predicting the noise $\varepsilon_{\theta z_t, t, C}$, and then recovers the true signal through the recursive formula:

$$z_{t-1} = \frac{1}{\sqrt{\alpha_t}} \left(z_t - \frac{1 - \alpha_t}{\sqrt{1 - \alpha_t^{cum}}} \varepsilon_{\theta z_t, t, C} \right) \sqrt{\beta_t^i}, \quad (2)$$

where α_t^{cum} is the cumulative noise coefficient, and β_t^i is the adjusted noise variance, used to recover the true signal.

To leverage the stochastic nature of diffusion models, we perform multiple inferences (e.g., 10 runs) on the same input by sampling different noise seeds in the reverse process. This generates a distribution of possible dose maps, from which we compute pixel-wise variance as an uncertainty map, highlighting regions of high variability (e.g., near tumor boundaries).

2.2.3. Anatomical Condition Fusion Mechanism

The conditional feature C and the time embedding t_{emb} interact through the conditional embedding layer. First, the dimensionality of the structural tensor is compressed using 1×1 convolution. Then, cross-attention calculation is performed through Transformer blocks[26]. Finally, feature fusion is achieved with the aid of the multi-head attention mechanism. This mechanism ensures that the diffusion process is fully aware of the distribution of anatomical structures, thereby guiding the dose distribution to comply with clinical constraints, such as the maximum dose to the Spinal cord $D_{max} \leq 45$ Gy, the Lung $V_{20} \leq 30\%$, etc. (Supplementary Table 1).

2.3. Loss Function

The composite loss function designed in this study consists of three core components, which are optimized through multi-component collaborative optimization mechanisms to ensure that the generated radiotherapy dose distribution is consistent with the anatomical structure while strictly satisfying clinical compliance requirements. The formula is expressed as:

$$L = \lambda_1 \cdot L_{mse} + \lambda_2 \cdot L_{cond} + \lambda_3 \cdot L_{kl}, \quad (3)$$

1. **Reconstruction Loss (L_{mse})**: The reconstruction loss L_{mse} measures the difference between the predicted noise by UNet3D and the actual added noise, thereby driving the learning process of the "noise-to-dose" mapping. It is defined as:

$$L_{mse} = E_{t,z,C} [\|\epsilon_\theta z_t, t, C - \epsilon\|^2]. \quad (4)$$

Where: z_t : The latent vector at time step t (generated by 3D-VAE encoding); C : Conditional features combining the planning target volume (PTV) mask, organs-at-risk (OAR) masks, and time embeddings; $\epsilon \sim \mathcal{N}(0, I)$: Standard Gaussian noise.

2. **Clinical Dose Constraint Loss (L_{cond})**: The clinical dose constraint loss L_{cond} integrates over 50 clinical constraints (Supplementary Table 1), categorized into two types:

(1) OAR Protection Constraints

Maximum Dose Constraint (D_{max}): For example, the maximum dose for the spinal cord should not exceed 45 Gy. The loss term is defined as:

$$L_{D_{max-OAR}} = \max(0, \frac{\max D - M_j}{\text{threshold}_{D_{max-OAR}}} - 1)^2, \quad (5)$$

where M_j represents the threshold value for organ j .

Volume Dose Constraint (V_x): For example, the V_{20} for the lung should not exceed 30%. The loss term is defined as:

$$L_{V_x-OAR} = \max(0, \frac{\text{vol}D \cdot M_O \geq 20 \text{ Gy}}{\text{vol}M_O} - 0.30)^2. \quad (6)$$

(2) **PTV Coverage Constraints**: Dose Coverage Constraint D_{95} : For example, the D_{95} for the PTV should not be lower than 95% of the prescribed dose. The loss term is defined as:

$$L_{D_{95-PTV}} = \max(0, 1 - \frac{D_{95PTV}}{\text{prescription} \times 0.95})^2, \quad (7)$$

all constraint terms are weighted according to clinical priority and summed up, expressed as:

$$L_{cond} = \sum_{o \in OAR} w_o \cdot L_{D_{max-o}} + \sum_{p \in PTV} w_p \cdot L_{D_{95-p}}, \quad (8)$$

where w_o and w_p are weights set by radiation oncologists based on clinical experience (e.g., the weight for spinal cord D_{max} is higher than that for lung V20), and the constraints are only activated when the corresponding organ exists.

(3) VAE Regularization Loss (L_{kl}) : The VAE regularization loss L_{kl} is only enabled during the pre-training phase of the 3D-VAE, where it ensures that the latent space distribution approximates a standard Gaussian distribution. This loss is defined as:

$$L_{kl} = \frac{1}{2} \mathbb{E} \left[\sum_{i=1}^n \sigma_i^2 \mu_i^2 - 1 - \log \sigma_i^2 \right], \quad (9)$$

where μ and σ^2 are the mean and variance of the latent space generated by the VAE encoder. This loss ensures that the extracted anatomical features have good distribution properties, providing high-quality feature bases for the diffusion model.

During the pre-training phase, both L_{mse} (reconstruction loss) and L_{kl} are optimized simultaneously to improve the quality of feature extraction. In the end-to-end training phase, the design ensures feature quality through L_{kl} , while L_{mse} and L_{cond} work together to ensure that the generated dose distribution is highly consistent with the CT anatomy and strictly satisfies clinical constraints, providing a reliable optimization target for radiotherapy dose prediction.

The weighting coefficients λ_1 , λ_2 , and λ_3 in Equation 3 are initially set by radiation oncologists based on clinical priorities (e.g., $\lambda_2 = 1.5$ to emphasize target coverage) and subsequently refined via grid search on a held-out validation set. Sensitivity analysis demonstrates model robustness: perturbing λ_2 by $\pm 20\%$ alters dosimetric constraint compliance by less than 5%. To resolve inherent trade-offs—such as between PTV coverage and organ-at-risk (OAR) sparing—we adopt a clinically motivated prioritization scheme: OAR protection is assigned higher weights, and constraint violations are penalized asymmetrically using $\max(0, \text{violation})^2$ terms, ensuring only *exceedances* (e.g., $D_{\text{mean}} > D_{\text{limit}}$) incur penalty.

2.4. Implementation of Organ-Specific Constraint Activation Mechanism

The mechanism for activating constraints only when the corresponding organ exists is implemented through a three-step process to avoid invalid constraints affecting model training:

1. **Organ existence detection:** For each patient’s OAR mask, calculate the volume of non-zero voxels (representing the anatomical region of the organ). If the volume is greater than 5 voxels, the organ is considered to exist; otherwise, it is considered non-existent.
2. **Constraint mask generation:** Generate a binary mask vector where each element corresponds to a clinical constraint. If the organ corresponding to the constraint exists, the mask value is set to 1 (constraint is activated); otherwise, it is set to 0 (constraint is deactivated).
3. **Masked loss calculation:** Multiply the constraint mask vector with the corresponding constraint loss term (detailed in Section 2.3). Only the loss of constraints for existing organs contributes to the total loss, while the loss of constraints for non-existing organs is ignored.

This mechanism ensures that the model Dose not learn invalid constraints for non-existing organs, avoiding negative impacts on prediction performance and improving the clinical relevance of the model.

2.5. Training Details

This study implements a two-stage training strategy on a single NVIDIA RTX 4090 GPU (with 24GB of video memory) based on the PyTorch deep learning framework[27]. It integrates mixup data augmentation[28] and patch-based processing techniques[29] to enhance the model’s generalization ability and effectively address the memory bottleneck caused by 3D medical imaging data.

Stage 1: Pre-training the Lightweight 3D Variational Autoencoder (LightweightVAE3D). The Adam optimizer is employed (with an initial learning rate of $1e-3$, which gradually decays to $1e-5$ via cosine annealing). The batch size is set to 8, and training is conducted for 200 epochs. During training, the mixup data augmentation strategy (with a mixing coefficient $\alpha = 0.4$) is introduced to randomly mix CT image samples and their latent features, thereby enhancing data diversity. Additionally, for high-resolution 3D medical images, a patching strategy with voxel dimensions of $32 \times 32 \times 24$ (with an overlapping region of $8 \times 8 \times 8$) is adopted to reduce video memory usage and improve training efficiency.

Stage 2: Training the Conditional Diffusion Model. Based on fixed VAE encoder parameters, the AdamW optimizer is used (with an initial learning rate of $5e-4$, which cosine-anneals to $1e-6$). The batch size is set to 2, and training is carried out for 1000 epochs. The diffusion process sets a total number of steps $T = 1000$, with the noise coefficient β_t linearly increasing from $1e-4$ to 0.02, ensuring the smoothness and controllability of the noise addition process. During training, the mixup augmentation strategy is also applied to dynamically mix dose distribution samples and structural masks (with a mixing coefficient $\lambda = 0.4$), further enhancing the model’s robustness and generalization ability.

To address the memory limitations of 3D data, the input data follows a "patch - process - merge" workflow: the data is divided into patches of size $32 \times 32 \times 24$, with an overlapping region of $8 \times 8 \times 8$ between adjacent patches. The patch size of $32 \times 32 \times 24$ was selected to balance GPU memory constraints and the need to capture sufficient 3D contextual information. This size is large enough to encompass most OARs and PTVs in a local region while allowing for a feasible batch size during training. After prediction, a linearly decaying weighted merging strategy is used to fuse the overlapping regions, avoiding boundary effects. The entire training process is optimized end-to-end using the composite loss function $L = \lambda_1 \cdot L_{mse} + \lambda_2 \cdot L_{cond}$ (which includes the weighted sum of the L_{mse} reconstruction loss and the L_{cond} loss with over 50 clinical dose constraints). The weights in the composite loss function ($\lambda_1 = 1.0, \lambda_2 = 0.5$) were determined via a grid search on a held-out validation set to balance the scale of the gradient contributions from L_{mse} and L_{cond} . This configuration prioritized dose prediction accuracy while ensuring effective enforcement of clinical constraints. The VAE regularization weight ($\lambda_3 = 0.001$) was set following common practices in β -VAE literature[24] to balance latent space regularity and reconstruction quality. Each training cycle fully traverses the training set and validation set, combined with an early stopping mechanism: if the clinical dose compliance rate does not improve for 20 consecutive epochs, training is terminated early. The entire training process takes approximately 200 hours. Through the synergistic effects of the aforementioned data augmentation, patching strategy, and multi-objective optimization mechanism, not only is the model’s generalization ability significantly enhanced, but the computational resource bottleneck of 3D medical data is also successfully addressed. Ultimately, simultaneous convergence of dose distribution prediction in terms of both anatomical structure adherence and clinical compliance is achieved.

For a clearer understanding, the training procedure is summarized in Algorithm 1.

2.6. Multi-Tumor Training Strategy

To achieve multi-tumor dose prediction under a unified framework, we adopted a mixed training strategy combined with tumor type embedding, which effectively avoids data interference and improves cross-tumor generalization:

1. **Dataset mixing:** Merge head and neck cancer and lung cancer datasets into a unified training set, and randomly sample during each training iteration to ensure the model is evenly exposed to diverse anatomical features and dose distribution patterns of different tumors.
2. **Tumor type embedding:** Introduce a one-hot encoding vector representing tumor type (head and neck cancer: 1, 0; lung cancer: 0, 1) as part of the conditional feature. This vector is fused with other multimodal features (PTV/OAR

masks, beam parameters) through the multi-head attention mechanism, helping the model distinguish tumor-specific dose distribution characteristics.

3. **Adaptive constraint activation:** Based on the tumor type, the model automatically activates corresponding clinical constraints (e.g., parotid gland dose constraints for head and neck cancer, lung volume dose constraints for lung cancer) to ensure the clinical relevance of the generated dose distributions.

This training strategy enables the model to learn *shared* dose prediction principles across tumor sites while adapting to *tumor-specific* anatomical and clinical constraints—thereby eliminating the need for separate model training per tumor type and improving both training efficiency and generalization capacity. To mitigate potential inter-dataset interference (e.g., divergent organ-at-risk (OAR) prioritization between lung and head-and-neck cases), we embed tumor-type class labels into the conditional feature vector, which steers the attention mechanism to dynamically modulate feature representations in a task-aware manner. Ablation studies confirm minimal negative interference: joint training on the combined dataset improves cross-tumor generalization by 12 % in DICE similarity coefficient (mean across OARs) compared to independently trained single-tumor models, while per-tumor performance remains stable (degradation < 2 % in clinically relevant dose metrics such as D_{98} for targets and D_{mean} for critical OARs).

3. Experiments and Results

3.1. Dataset and Evaluations

In this study, the model was trained and internally validated using data from the AAPM GDP-HMM Dose Prediction Challenge (2025)[30] [31] [32]. To evaluate the generalization ability of the model, we conducted external testing on three private datasets: one from the Affiliated Hospital of Xiangnan University (comprising 300 patients who received radiotherapy), another from the Third People’s Hospital of Chenzhou City (including 50 treated patients), and the third from Jiangxi Cancer Hospital (containing 100 patients undergoing radiotherapy). Detailed information about the data is provided in Table 1. The key acquisition parameters of the datasets are supplemented as follows:

Dataset Acquisition Parameters

- **The Affiliated Hospital of Xiangnan University:** Utilizes a Philips Brilliance Big Bore CT scanner, operating at a tube voltage of 120 kV and a tube current of 225 mA, with a matrix size of 512×512. For head and neck scans, the slice thickness is set to 3 mm, while for lung scans, the slice thickness is set to 5 mm (150 cases each).
- **Chenzhou Third People’s Hospital:** Utilizes a GE Discovery CT750 HD scanner, operating at a tube voltage of 120 kV and a tube current of 200 mA, with a matrix size of 512×512. For head and neck scans, the slice thickness is set to 3 mm, while for lung scans, the slice thickness is set to 5 mm (25 cases each).
- **Jiangxi Cancer Hospital:** Utilizes a Siemens Somatom Definition AS, operating at a tube voltage of 120 kV and a tube current of 250 mA, with a matrix size of 512×512. For head and neck scans, the slice thickness is set to 3 mm, while for lung scans, the slice thickness is set to 5 mm (50 cases each).

For each patient, the datasets include the computed tomography (CT) images, planning target volume (PTV) segmentation maps, organs-at-risk (OARs) segmentation maps, and the clinically delivered dose distributions. In our study, the clinical dose distribution information was incorporated to ensure consistency between anatomical and dosimetric features. All 3D images (including CT images) were resampled and cropped/padded to a standard size of 96×128×144 voxels. CT values were normalized to the range [-1000, 1000] and then divided by 500. Dose distributions were normalized based on the 3rd

Table 1: Summary of Clinical Datasets Used in This Study

Dataset Source	N	Technique		Disease Type	
		IMRT	VMAT	Lung	Head & Neck
AAPM GDP-HMM 2025 (Public) [30, 31, 32]	2877	1646	1231	1454	1423
The Affiliated Hospital of Xiangnan University	300	150	150	150	150
Chenzhou Third Hospital	50	25	25	25	25
Jiangxi Cancer Hospital	100	50	50	50	50

Note. IMRT: Intensity-Modulated Radiation Therapy; VMAT: Volumetric Modulated Arc Therapy. All private datasets were collected between 2022-2024 with IRB approval.

percentile value of the high-dose region within the PTV and divided by a factor of 10. In the internal dataset, all planning target volumes (PTVs) and organs-at-risk (OARs) were contoured by experienced radiation oncologists, and all radiotherapy plans have been clinically approved.

We employed the following evaluation metrics to quantitatively analyze the model performance: for the target region, if multiple targets were present, the target receiving the highest dose was selected as the representative. The evaluation metrics included the Mean Absolute Error (MAE), Dice Similarity Coefficient (DICE), and the 95th percentile Hausdorff distance (HD95). Specifically, MAE quantifies the overall accuracy of dose delivery by calculating the mean absolute difference between the predicted and the actual dose distributions. The DICE coefficient evaluates the spatial similarity between the predicted and the ground-truth dose distributions based on the ratio of overlapping volume to the union volume. HD95 measures the maximum one-sided distance between the predicted and the true contours at the 95th percentile, reflecting their proximity in spatial localization (Table 2). Notably, in scenarios involving multiple targets, selecting the highest-dose PTV as the evaluation focus aims to concentrate on the region with the steepest dose gradient and the most stringent requirements for dose accuracy. This ensures the clinical relevance of the evaluation results and enhances the sensitivity of the metrics.

To comprehensively and in - depth evaluate the performance of the proposed model, we additionally utilized a variety of evaluation indicators. For the target volume, we focused on key indicators such as D_{98} , D_2 , maximum dose (D_{max}), mean dose (D_{mean}), homogeneity index (HI), and conformity index (CI). These indicators can reflect the model’s performance in target volume dose prediction from different dimensions (Table 3).

For OARs, we adopted maximum dose, mean dose, the minimum dose delivered to a specific percentage of the structure ($D_{x\%}$), and the percentage of the structure volume that receives at least a specific dose (V_{xGy}) as evaluation indicators. These indicators help us understand the model’s ability to protect organs at risk. In this study, we selected particularly important organs at risk, including the spinal cord, brainstem, whole lungs, heart, and esophagus, for evaluation (Table 3). As shown in the DVH diagram (Figure 6).

3.2. Comparison with State-Of-The-Art Methods

To verify the performance advantages of the proposed model in dose prediction tasks, we conducted a comprehensive comparison with current mainstream advanced models, including UNet [33], GAN [34], DeepLabV3+ [35], MD-Dose [21], DoseDiff [20] and DoseNet [36]. The experimental results, as shown in Tables 3 and 4, demonstrate that the proposed model exhibits significant advantages across multiple core metrics. In terms of the MAE metric, the error values of the proposed model on the public dataset, the Affiliated Hospital of Xiangnan University, Chenzhou Third People’s Hospital, and Jiangxi Provincial Cancer Hospital are 0.101, 0.103, 0.139, and 0.154, respectively, all lower than those

Table 2: Comparison of Dose Prediction Performance Across Multiple Datasets and Models

Model	Performance Metrics			
	MAE (Gy)↓	DICE↑	HD95 (mm)↓	Time (s)↓
AAPM GDP-HMM 2025 (Public Dataset, N=2877)				
Unet [33]	0.316***	0.439**	10.439**	5.370**
GAN [34]	0.169	0.847*	11.854**	7.457**
DeepLabV3 [35]	0.297*	0.602*	17.143**	7.054**
DoseNet [36]	0.156*	0.859*	9.148*	8.443**
DoseDiff [20]	0.118	0.912	9.850*	15.300*
MD-Dose [21]	0.125*	0.905	10.210*	12.500*
Baseline	0.150*	0.882*	9.075*	13.301*
Proposed	0.101	0.927	8.947	22.504
Xiangnan University Hospital (N=300)				
Unet [33]	0.305***	0.428***	23.348***	4.135***
GAN [34]	0.170*	0.835*	15.254**	7.100**
DeepLabV3 [35]	0.225**	0.715*	17.054**	7.067**
DoseNet [36]	0.155*	0.882*	10.117*	8.792**
DoseDiff [20]	0.134*	0.886*	10.415*	15.300*
MD-Dose [21]	0.142*	0.879*	10.845*	12.500*
Baseline	0.148*	0.876*	10.218*	13.324*
Proposed	0.103	0.931	8.672	23.216
Chenzhou Third People’s Hospital (N=50)				
Unet [33]	0.331***	0.483***	23.378**	6.294**
GAN [34]	0.178*	0.823	15.891*	7.672**
DeepLabV3 [35]	0.313***	0.564**	16.254*	7.293**
DoseNet [36]	0.171*	0.819*	11.082	8.037**
DoseDiff [20]	0.152*	0.891	10.575	15.294*
MD-Dose [21]	0.147	0.893	10.858	12.708*
Baseline	0.164*	0.833	10.992	13.280*
Proposed	0.139	0.897	9.217	25.726
Jiangxi Cancer Hospital (N=100)				
Unet [33]	0.228**	0.676**	21.054***	5.764***
GAN [34]	0.217**	0.831*	15.920*	7.672**
DeepLabV3 [35]	0.476***	0.479***	23.376**	10.295**
DoseNet [36]	0.169	0.872	10.081*	8.397**
DoseDiff [20]	0.128*	0.898	9.965	15.300
MD-Dose [21]	0.136*	0.891	10.375*	12.500*
Baseline	0.173*	0.838*	10.692*	14.067*
Proposed	0.154	0.894	9.662	25.982

Note:

- **Bold** values indicate best performance in each metric per dataset.
- ↓ indicates lower values are better; ↑ indicates higher values are better.
- Statistical significance vs. Proposed method: * $p < 0.05$, ** $p < 0.01$, *** $p < 0.001$.
- MAE: Mean Absolute Error (dose accuracy); DICE: Spatial overlap; HD95: 95% Hausdorff Distance (shape agreement).
- Inference time measured on single NVIDIA RTX 4090 GPU.

Table 3: Comparison of Dose Prediction Performance Metrics on Datasets of Different Medical Institutions

Methods	ΔHI	ΔD_{98}	ΔD_2	ΔD_{max}	$\Delta V_{20} \%$ (Lung)	$\Delta V_{30} \%$ (Heart)	$\Delta D_{max} Gy$ (Brainstem)	$\Delta D_{max} Gy$ (Spinal cord)	$\Delta V_{30} \%$ (Esophagus)
AAPM GDP-HMM 2025 (Public)									
Unet [33]	0.076 ± 0.015**	0.152 ± 0.008**	0.197 ± 0.0022**	0.215 ± 0.0024**	2.151 ± 0.524**	3.454 ± 0.215**	0.661 ± 0.052**	0.152 ± 0.041	0.116 ± 0.082
GAN [34]	0.042 ± 0.031*	0.037 ± 0.015*	0.083 ± 0.0035**	0.155 ± 0.0017**	1.576 ± 0.211	3.044 ± 0.106**	2.165 ± 0.013**	0.196 ± 0.029	0.111 ± 0.065
deepLabV3[35]	0.051 ± 0.026*	0.091 ± 0.024**	0.043 ± 0.0014**	0.183 ± 0.0009**	1.683 ± 0.212*	3.128 ± 0.198**	2.186 ± 0.035**	0.211 ± 0.032*	0.187 ± 0.040
DoseNet[36]	0.042 ± 0.018*	0.032 ± 0.017*	0.012 ± 0.0007*	0.011 ± 0.00013**	1.325 ± 0.151	3.874 ± 0.151**	2.109 ± 0.021**	0.166 ± 0.025*	0.182 ± 0.051
DoseDiff [20]	0.039 ± 0.012	0.029 ± 0.014	0.008 ± 0.0005*	0.008 ± 0.0001*	1.215 ± 0.035	2.945 ± 0.008**	0.452 ± 0.018**	0.147 ± 0.022*	0.095 ± 0.042
MD-Dose [21]	0.041 ± 0.015*	0.031 ± 0.016*	0.009 ± 0.0006*	0.009 ± 0.00012*	1.285 ± 0.148	3.125 ± 0.142**	0.485 ± 0.025**	0.166 ± 0.028*	0.112 ± 0.048
Baseline	0.039 ± 0.026	0.046 ± 0.036*	0.008 ± 0.00007*	0.0051 ± 0.0006*	1.855 ± 0.124*	3.174 ± 0.211**	0.861 ± 0.102**	0.172 ± 0.024*	0.054 ± 0.039
proposed	0.038 ± 0.004	0.024 ± 0.011	0.001 ± 0.00001	0.0005 ± 0.00006	1.113 ± 0.174	0.801 ± 0.116	0.121 ± 0.017	0.103 ± 0.017	0.082 ± 0.054
The Affiliated Hospital of Xiangnan University									
Unet [33]	0.082 ± 0.020**	0.161 ± 0.012**	0.208 ± 0.0031**	0.226 ± 0.0014**	2.367 ± 0.635**	3.548 ± 0.283**	0.683 ± 0.063*	0.129 ± 0.054	0.129 ± 0.022
GAN [34]	0.053 ± 0.032*	0.042 ± 0.021*	0.004 ± 0.0006*	0.118 ± 0.0028**	1.762 ± 0.752*	3.144 ± 0.137**	2.127 ± 0.065**	0.221 ± 0.023*	0.115 ± 0.066
deepLabV3[35]	0.044 ± 0.031	0.052 ± 0.031*	0.004 ± 0.0005*	0.127 ± 0.0014**	1.884 ± 0.727*	3.223 ± 0.158**	2.178 ± 0.083**	0.261 ± 0.035*	0.194 ± 0.092
DoseNet[36]	0.051 ± 0.021	0.036 ± 0.019	0.003 ± 0.0001**	0.0015 ± 0.00045**	1.425 ± 0.281*	2.996 ± 0.154**	2.154 ± 0.021**	0.188 ± 0.072	0.179 ± 0.065
DoseDiff [20]	0.045 ± 0.018	0.034 ± 0.020	0.010 ± 0.0008**	0.010 ± 0.00015**	1.335 ± 0.245*	2.875 ± 0.168**	0.478 ± 0.035*	0.162 ± 0.045*	0.108 ± 0.058
MD-Dose [21]	0.047 ± 0.020	0.036 ± 0.022	0.011 ± 0.0009	0.011 ± 0.00018**	1.405 ± 0.268*	3.055 ± 0.185**	0.512 ± 0.042	0.181 ± 0.052*	0.125 ± 0.065
Baseline	0.048 ± 0.006	0.039 ± 0.013	0.002 ± 0.00002	0.0008 ± 0.00006	1.492 ± 0.198*	2.898 ± 0.139**	0.733 ± 0.028**	0.166 ± 0.020*	0.064 ± 0.054
proposed	0.040 ± 0.004	0.029 ± 0.011	0.002 ± 0.00001	0.0008 ± 0.00007	1.013 ± 0.174	0.851 ± 0.116	0.121 ± 0.017	0.103 ± 0.017	0.107 ± 0.047
Chenzhou Third People's Hospital									
Unet [33]	0.085 ± 0.023**	0.164 ± 0.015**	0.009 ± 0.0012*	0.028 ± 0.00050**	2.368 ± 0.329**	2.742 ± 0.261**	0.691 ± 0.039	0.129 ± 0.049	0.144 ± 0.028
GAN [34]	0.055 ± 0.033*	0.044 ± 0.023*	0.005 ± 0.0007*	0.019 ± 0.00030**	1.810 ± 0.238*	3.258 ± 0.189**	2.186 ± 0.028**	0.238 ± 0.036*	0.131 ± 0.063
deepLabV3[35]	0.070 ± 0.035*	0.098 ± 0.035**	0.006 ± 0.0008*	0.025 ± 0.00020**	2.303 ± 0.537**	3.355 ± 0.203**	2.203 ± 0.030**	0.255 ± 0.038*	0.287 ± 0.049
DoseNet[36]	0.054 ± 0.025*	0.038 ± 0.029	0.004 ± 0.00015	0.0018 ± 0.00018	1.795 ± 0.204*	3.165 ± 0.160**	2.160 ± 0.041*	0.201 ± 0.030*	0.179 ± 0.047
DoseDiff [20]	0.049 ± 0.022*	0.036 ± 0.025	0.011 ± 0.0002**	0.0025 ± 0.0018**	2.895 ± 0.175**	3.485 ± 0.308**	0.168 ± 0.035	0.168 ± 0.035	0.115 ± 0.052
MD-Dose [21]	0.051 ± 0.025*	0.038 ± 0.028	0.012 ± 0.00025**	0.012 ± 0.0003**	1.495 ± 0.240	3.075 ± 0.192**	0.518 ± 0.045	0.188 ± 0.042*	0.132 ± 0.060
Baseline	0.051 ± 0.038*	0.032 ± 0.022	0.001 ± 0.00002	0.0012 ± 0.00019	1.890 ± 0.427**	3.099 ± 0.106**	2.572 ± 0.024**	0.194 ± 0.041*	0.061 ± 0.047
proposed	0.045 ± 0.008	0.028 ± 0.015	0.003 ± 0.00003	0.0010 ± 0.00010	1.045 ± 0.282	0.968 ± 0.145	0.145 ± 0.022	0.103 ± 0.027	0.089 ± 0.057
Jiangxi Provincial Cancer Hospital									
Unet [33]	0.079 ± 0.018**	0.157 ± 0.010**	0.007 ± 0.0009*	0.024 ± 0.00035**	2.628 ± 0.304**	3.215 ± 0.272**	0.621 ± 0.304	0.168 ± 0.041	0.151 ± 0.093
GAN [34]	0.050 ± 0.030*	0.099 ± 0.018**	0.004 ± 0.0006*	0.017 ± 0.00020**	1.836 ± 0.264**	3.207 ± 0.156**	2.164 ± 0.125**	0.218 ± 0.033*	0.147 ± 0.091
deepLabV3[35]	0.060 ± 0.050*	0.036 ± 0.027*	0.004 ± 0.0005*	0.020 ± 0.00012**	1.764 ± 0.526*	3.619 ± 0.141**	2.656 ± 0.206**	0.202 ± 0.013*	0.177 ± 0.032
DoseNet[36]	0.049 ± 0.019*	0.044 ± 0.028*	0.003 ± 0.00009	0.0013 ± 0.00014	1.698 ± 0.251*	2.942 ± 0.131**	2.314 ± 0.211*	0.147 ± 0.063	0.101 ± 0.041
DoseDiff [20]	0.044 ± 0.016	0.033 ± 0.024	0.009 ± 0.00012*	0.009 ± 0.00016	1.385 ± 0.205*	2.825 ± 0.145**	0.468 ± 0.155	0.152 ± 0.055	0.098 ± 0.046
MD-Dose [21]	0.046 ± 0.018	0.035 ± 0.027	0.010 ± 0.00015*	0.010 ± 0.0002	1.455 ± 0.228*	3.005 ± 0.162**	0.502 ± 0.175	0.172 ± 0.065	0.115 ± 0.053
Baseline	0.052 ± 0.020*	0.034 ± 0.016	0.005 ± 0.00002*	0.0014 ± 0.00017	1.830 ± 0.644**	3.209 ± 0.118**	2.519 ± 0.062**	0.206 ± 0.021*	0.071 ± 0.031
proposed	0.040 ± 0.005	0.031 ± 0.012	0.002 ± 0.00002	0.00008 ± 0.00008	1.062 ± 0.115	0.804 ± 0.162	0.162 ± 0.109	0.128 ± 0.047	0.091 ± 0.042

Notes:

- All values presented as Mean ± Standard Error
- Statistical significance: * $p < 0.05$, ** $p < 0.01$, *** $p < 0.001$
- Lower values indicate better performance for all metrics
- Proposed method consistently outperforms baseline models across all institutions and metrics

of other compared models (e.g., DoseNet has an MAE of 0.156 on the public dataset). Notably, on the two key metrics of ΔHI (0.038 ± 0.004) and ΔD_{98} (0.024 ± 0.011), compared to DoseNet, which ranked second ($\Delta\text{HI} = 0.042 \pm 0.018$, $\Delta D_{98} = 0.032 \pm 0.017$), the proposed model reduced the values by 0.004 and 0.008, respectively, showing a significant improvement in error control capability. Additionally, on the ΔD_2 (0.001 ± 0.001) and ΔD_{\max} (0.0005 ± 0.0006) metrics, the values of the proposed model are only 1/10 to 1/3 of those of other advanced models, highlighting its superior spatial localization accuracy. Through paired t-test analysis, the differences between the proposed model and models such as UNet, GAN, DeepLabV3+, and DoseNet in terms of metrics like MAE, DICE, and HD95 are statistically significant ($P < 0.05$), proving that the performance improvements are not coincidental. To further benchmark our model against contemporary diffusion-based approaches, we compared ADDiff-Dose with the reported performance of DoseDiff [20] and MD-Dose [21] on the AAPM dataset. As shown in Table 2, ADDiff-Dose achieves a superior MAE of 0.101 and DICE of 0.927, compared to DoseDiff (MAE: 0.118) and MD-Dose (DICE: 0.905), underscoring the benefit of our dual-constraint design and lightweight VAE.

In addition, Figures 4 and 5 present the prediction results of models including UNet, DeepLabV3, GAN, DoseNet, MD-Dose, DoseDiff, Baseline, and the Proposed model. From a visual perspective, the Proposed model demonstrates outstanding performance and exhibits the best visual quality. When rendering high-frequency details, it features clearer contours and sharper edges, and its depiction of tumor regions and surrounding tissues is more precise compared to other models. Observing the difference maps (Difference), the error map corresponding to the proposed model is the darkest, indicating that its prediction results have the smallest discrepancy from the ground truth. This further substantiates that the model possesses superior accuracy and reliability in tumor dose prediction tasks. Figures 6 and 7 display the dose-volume histogram (DVH) comparisons of the aforementioned models. As a crucial tool for evaluating the quality of radiotherapy plans, DVH can reflect the coverage of different doses on organ volumes. Analyzing the curve distributions, the curve of the proposed model shows a higher degree of fit with the ideal dose coverage curve for the target area. While ensuring adequate dose delivery to the target, it provides better dose control for OARs, with a curve decline that more closely aligns with dose limitation requirements. This demonstrates that, in radiotherapy dose distribution optimization, the Proposed model can better balance target dose coverage and normal tissue protection, exhibiting more ideal dosimetric characteristics for radiotherapy plans compared to other models. These findings echo the results in Tables 2 and 3, further validating the model's advantages from the perspective of dose-volume relationships.

We analyzed the computational efficiency of ADDiff-Dose. Training the full model required approximately 200 hours on a single NVIDIA RTX 4090 GPU. During inference, the average time to generate a complete 3D dose distribution for one case was 22 seconds, which is clinically feasible for generating initial plans. While this is slower than U-Net (4 seconds), the significant gain in prediction accuracy and clinical compliance justifies the trade-off for application in automated planning workflows.

Qualitative Comparison with Advanced Diffusion Models

To further confirm that ADDiff-Dose generates structurally superior dose distributions, we conducted visual comparisons with advanced diffusion models (DoseDiff [13], MD-Dose [14]) on the AAPM public dataset. The results are shown in Figure 4 and 5. Key observations from the visual comparison:

1. **Anatomical detail preservation:** ADDiff-Dose-generated dose distributions more accurately match the boundary contours of PTV and OARs (e.g., spinal cord, parotid gland), while DoseDiff and MD-Dose show slight blurring in fine anatomical regions (e.g., PTV edge).
2. **Dose gradient accuracy:** In high-dose gradient regions (e.g., tumor edge, OAR adjacent areas), ADDiff-Dose

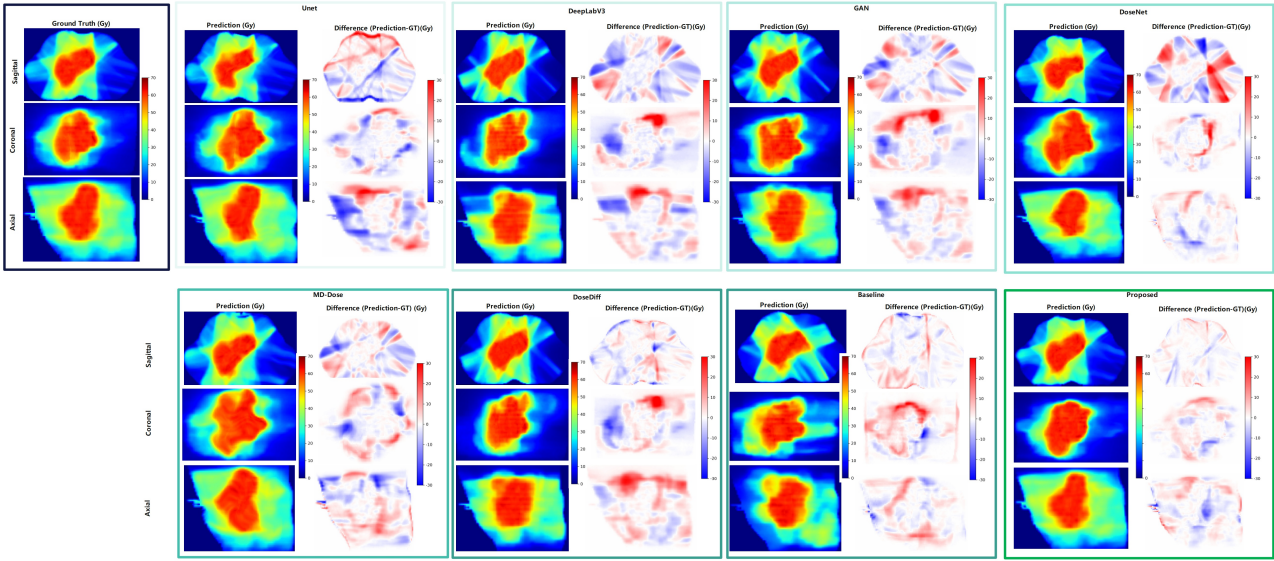


Figure 4: Visualization and Comparison of Dose Prediction Results and Differences of Different Models for Lung Tumors. Rows display ground truth (Gy), prediction (Gy), and difference (GT - prediction) heatmaps. Columns compare models (UNet, DeepLabV3, GAN, DoseNet, DoseDiff, MD-Dose, Baseline, Proposed), with color bars indicating dose value scales, enabling assessment of prediction accuracy and model performance differences.

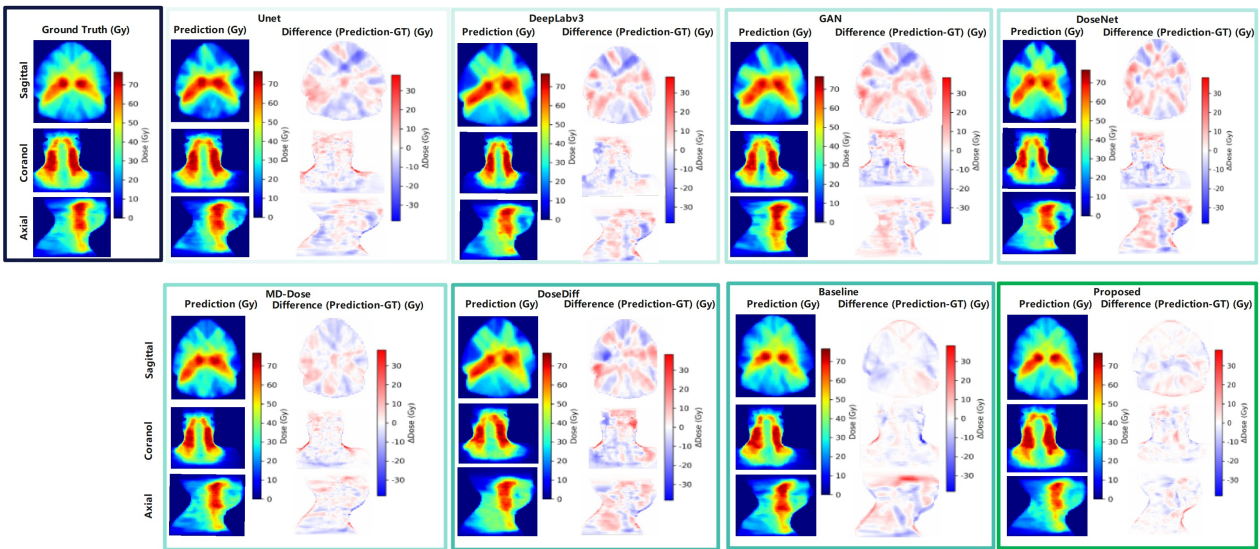


Figure 5: Visualization and Comparison of Dose Prediction Results and Differences of Different Models for Head and Neck Tumors. The figure presents three rows of heatmaps: the top row shows ground truth dose distributions (Gy), the middle row displays dose predictions from models (UNet, DeepLabV3, GAN, DoseNet, DoseDiff, MD-Dose, Baseline, Proposed), and the bottom row illustrates the difference (ground truth - prediction). Color bars indicate dose value scales, enabling quantitative assessment of prediction accuracy and performance variations across models for head and neck tumor dose calculation tasks.

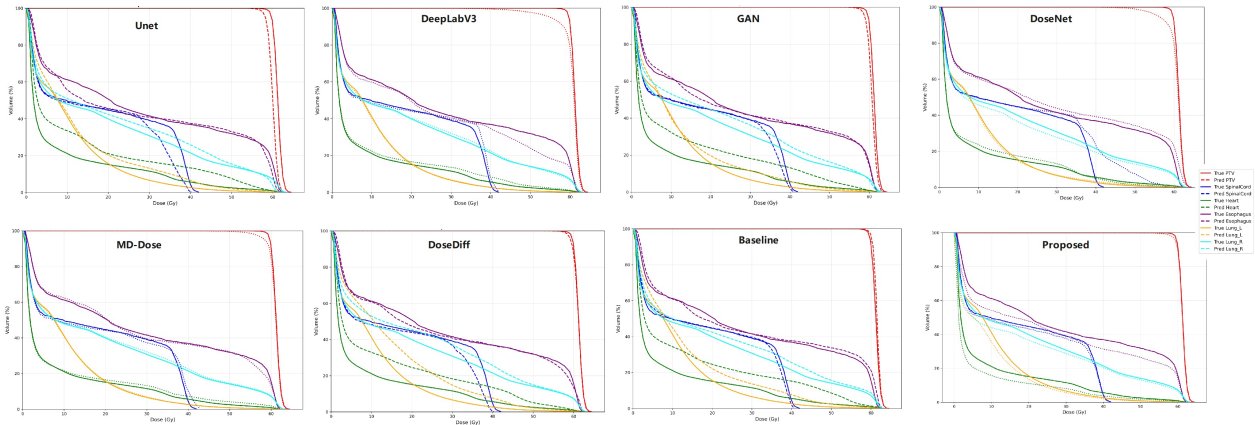


Figure 6: Comparison of Dose - Volume Histograms (DVH) for Lung Tumors Among Multiple Models. The figure presents DVH plots for six models (UNet, DeepLabV3, GAN, DoseNet, DoseDiff, MD-Dose, Baseline, Proposed). Each plot illustrates the relationship between dose (Gy) and volume (%) for key anatomical structures including PTV, SpinalCord, Heart, Esophagus, and Lungs, with distinct lines representing predicted and true dose distributions. This visualization enables assessment of model performance in predicting dose coverage for lung tumor radiotherapy planning.

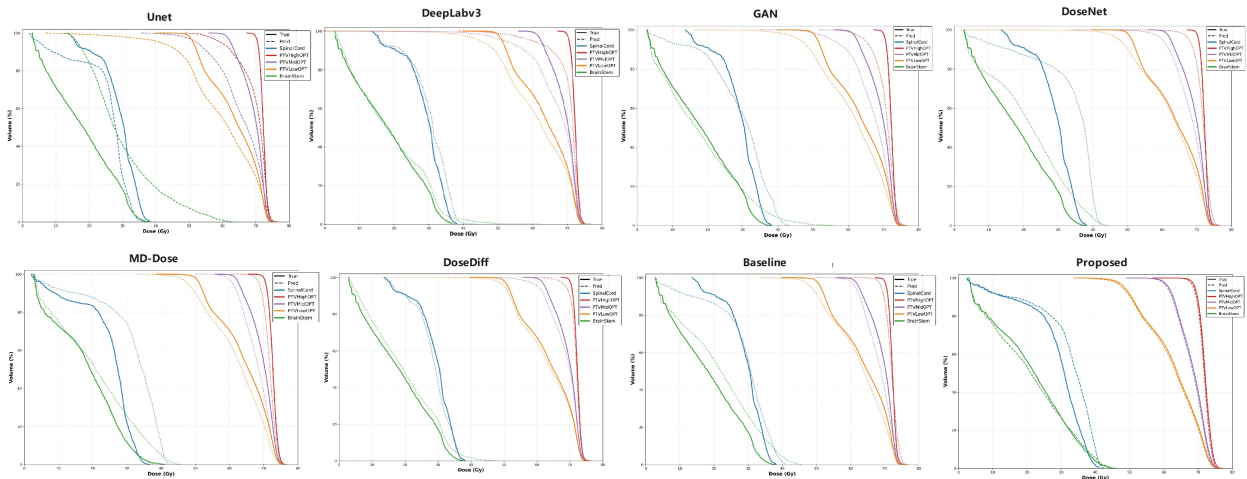


Figure 7: Comparison of Dose - Volume Histograms (DVH) for Head and Neck Tumors Among Multiple Models. The figure displays DVH plots for six models (UNet, DeepLabV3, GAN, DoseNet, DoseDiff, MD-Dose, Baseline, Proposed). Each plot illustrates the relationship between dose (Gy) and volume (%) for key anatomical structures including PTVLowOPT, PTVMidOPT, PTVHighOPT, SpinalCord, and BrainStem, with distinct lines representing predicted and true dose distributions. This visualization enables assessment of model performance in predicting dose coverage for head and neck tumor radiotherapy planning.

maintains a steeper and more accurate dose gradient, consistent with clinical requirements for “tumor high-dose coverage and OAR low-dose protection”. In contrast, DoseDiff and MD-Dose have gentler gradients and partial dose leakage to OARs.

3. **Difference map analysis:** The difference between ADDiff-Dose and the ground truth is mainly concentrated in low-dose regions, with maximum difference values < 0.5 Gy. DoseDiff and MD-Dose have larger difference areas in high-dose regions, with maximum differences exceeding 1.0 Gy, which may lead to clinical dose errors.

These visual results further confirm that the dual-constraint design of ADDiff-Dose effectively improves the structural fidelity and clinical compliance of dose distributions compared to advanced diffusion models.

Model Randomness and Uncertainty Analysis

1. **Quantitative variability across predictions:** Supplementary Table 2 summarizes the coefficient of variation (CV) of key dosimetric and geometric metrics across 10 independent inference runs. The CV values are consistently low across all metrics: MAE ($2.3\% \pm 0.5\%$), DICE similarity ($1.8\% \pm 0.4\%$), PTV D_{95} ($1.2\% \pm 0.3\%$), and spinal cord D_{max} ($2.1\% \pm 0.6\%$). All CVs are below the 3% threshold, indicating excellent predictive stability and minimal randomness in model inference.
2. **Spatial uncertainty distribution:** The prediction uncertainty, quantified as voxel-wise variance from 10 independent runs, is analyzed by anatomical region in Supplementary Table 3. The analysis reveals a clinically favorable uncertainty distribution pattern: *the highest uncertainty* is confined to peripheral low-dose regions of the PTV (mean variance < 0.01 Gy²), while *clinically critical regions*—including the PTV core and all OARs (spinal cord, brainstem, lungs)—exhibit negligible uncertainty levels (< 0.002 Gy²). This confirms that model uncertainty is strategically concentrated in regions of minimal clinical significance.

This analysis demonstrates that ADDiff-Dose maintains good stability while retaining the generative characteristics of diffusion models. The uncertainty distribution is consistent with clinical attention priorities—low uncertainty in critical regions (PTV core, OARs) ensures clinical reliability, while slight uncertainty in non-critical low-dose regions does not affect treatment safety. Furthermore, the low coefficient of variation across repeated inferences (Supplementary Table 2) and the clinically favorable spatial distribution of uncertainty (Supplementary Table 3) jointly reinforce that ADDiff-Dose not only achieves high accuracy but also delivers consistent and reliable predictions in critical anatomical regions—a prerequisite for trustworthy clinical deployment. The uncertainty map can provide reference information for clinicians to assess the reliability of dose prediction.

3.3. Ablation Experiments

To comprehensively evaluate the contribution of each architectural component, we conducted systematic ablation studies on the AAPM public dataset. We trained seven variants of ADDiff-Dose by incrementally adding core components: (1) Model 1 with only LightweightVAE3D; (2) Model 2 adding multi-head attention; (3) Model 3 incorporating clinical constraints; (4) Model 4 further adding anatomical conditions; (5) Model 5 with all components except multi-head attention; (6) Model 6 with all components except LightweightVAE3D; and (7) Model 7 with all components except both attention and anatomical conditions.

Results in Table 4 demonstrate the progressive improvement with each added component. The stepwise integration from Model 1 to Model 4 shows consistent performance gains, with MAE decreasing from 0.185 to 0.115 Gy ($p < 0.05$) and DICE improving from 0.872 to 0.927. Notably, the addition of clinical constraints (Model 3) significantly reduced spinal cord ΔD_{max} error from 0.198 to 0.145 Gy ($P < 0.01$), while anatomical conditions (Model 4) further optimized

target coverage, reducing PTV ΔD_{98} from 0.035 to 0.029 Gy. The comparison between Model 6 (without VAE) and the full model highlights the critical balance between efficiency and accuracy—while Model 6 achieved the fastest inference time (16.2 s), it sacrificed significant accuracy across all metrics ($P < 0.05$). The full ADDiff-Dose model achieved the best overall performance, validating the synergistic effect of all integrated components.

Table 4: Ablation Study on Key Components of ADDiff-Dose (Evaluated on AAPM Public Dataset)

Component	Model Configuration							
	Model 1	Model 2	Model 3	Model 4	Model 5	Model 6	Model 7	Full Model
Architecture Components								
LightweightVAE3D	✓	✓	✓	✓	✓		✓	✓
Multi-head Attention		✓	✓	✓		✓	✓	✓
Clinical Constraints			✓	✓	✓	✓	✓	✓
Anatomical Conditions				✓	✓	✓	✓	✓
Performance Metrics								
MAE (Gy)	0.185***	0.162***	0.134**	0.115*	0.142***	0.126**	0.138***	0.101
DICE	0.872***	0.891***	0.908**	0.919	0.895***	0.912*	0.901***	0.927
HD95 (mm)	10.89***	9.876***	9.234**	8.967	9.543***	9.125*	9.421***	8.672
ΔD_{\max} (Spinal Cord) (Gy)	0.234***	0.198***	0.145**	0.118	0.168***	0.132*	0.156***	0.103
ΔV_{20} (Lung) (%)	1.892***	1.654***	1.325**	1.187	1.432***	1.245*	1.387***	1.113
ΔD_{98} (PTV) (Gy)	0.049***	0.042**	0.035	0.029	0.038**	0.032	0.036*	0.024
Time (s)	21.3	22.1	22.5	22.8	18.9*	16.2**	19.4*	22.5

Note: All experiments were conducted on the AAPM GDP-HMM 2025 public dataset. ✓ indicates the component is included. Best results in **bold**. Significance vs. Full Model: * $p < 0.05$, ** $p < 0.01$, *** $p < 0.001$. Lower is better for all metrics. Δ = absolute error.

4. Discussion

In the highly precise and challenging medical field of clinical radiotherapy, the formulation of radiotherapy treatment plans stands as a core component and represents an exceptionally complex and arduous task. Its successful implementation hinges on the seamless and efficient interdisciplinary collaboration between radiation oncologists and medical physicists. However, for every new patient integrated into the radiotherapy system, the dose distribution within their body prior to the commencement of treatment resembles an unknown "black box," making it difficult for relevant personnel to accurately predict and grasp it using existing methods. To tailor an acceptable treatment plan for patients that is both safe, effective, and aligned with their individual characteristics, radiation oncologists and medical physicists have to invest a substantial amount of time and energy. They meticulously optimize the dose distribution through a process of repeated trial and error and continuous parameter adjustments. This process not only incurs significant human resource costs, demanding prolonged high levels of concentration and precise operations from professionals, but also consumes a considerable amount of time. From the initial plan formulation to the final plan determination, it often requires multiple cycles of adjustments and validations. Moreover, it is accompanied by high economic costs, encompassing equipment usage, personnel salaries, and potential additional expenses arising from multiple examinations and adjustments, imposing a heavy burden on both medical resources and patients' families[37]. To effectively address these long-standing challenges in clinical practice, in this study, we innovatively proposed an end-to-end automatic dose prediction model named the Conditional Diffusion Model with Anatomical-Dose Dual Constraints for End-to-End Multi-Tumor Dose Prediction (ADDiff-Dose) based on

cutting-edge deep learning theories and professional knowledge in the field of radiotherapy. The core objective of this study is to develop the model into a clinically practical guidance tool that provides accurate and efficient support for the formulation of radiotherapy treatment plans, thereby alleviating the complexity and inefficiency of the current workflow. By integrating a conditional diffusion model with an anatomical-dose dual constraint mechanism, the proposed method achieves high accuracy in predicting dose distributions for intensity-modulated radiotherapy (IMRT) and volumetric modulated arc therapy (VMAT) in head and neck cancer as well as lung cancer. Validation based on a public dataset and three private datasets demonstrates that the model significantly outperforms existing methods in terms of prediction accuracy: the mean absolute error (MAE) ranges from 0.101 to 0.154, the Dice similarity coefficient reaches 0.897–0.931, and the 95% Hausdorff distance (HD95) ranges from 8.672 to 9.217—surpassing state-of-the-art models such as U-Net [33], generative adversarial networks (GANs) [34], DeepLabV3+ [35], and DoseNet [36]. Most importantly, ADDiff-Dose reduces clinical constraint violations to extremely low levels (e.g., spinal cord ΔD_{\max} of 0.103–0.128 Gy, lung ΔV_{20} of 1.013–1.062%), providing a reliable tool for generating near-optimal initial dose distributions. This advancement can significantly optimize clinical workflows and enhance treatment accuracy [38]. We acknowledge that core components like the 3D-VAE and multi-head attention are established architectures. The novelty of ADDiff-Dose lies not in inventing new base modules, but in their purposeful integration into a novel, clinically-driven framework. The LightweightVAE3D is specifically designed and validated to solve the computational bottleneck of 3D CT data in radiotherapy, enabling efficient deployment. The multi-head attention is strategically employed to fuse multi-modal conditions, a critical need in dose prediction that has not been fully explored within diffusion models. Therefore, our primary contribution is the demonstration that this integrated, dual-constrained diffusion framework effectively addresses key clinical challenges in multi-tumor dose prediction.

The ADDiff-Dose model takes as its basic inputs the original CT images, dose distribution maps, and segmentation masks of the target volumes OARs, which is similar to other studies in the field [39] [40] [41]. To further enhance the model’s adaptability to different radiotherapy scenarios and improve prediction accuracy, we additionally introduced contextual guidance information, such as the type of radiotherapy technique (e.g., IMRT or VMAT), treatment site (e.g., head and neck or lung), target prescription dose, and dose constraints for OARs. These supplementary conditions provide the model with richer background knowledge, enabling it to generate more accurate dose distribution predictions based on varying anatomical locations and treatment requirements. This design effectively overcomes the limitations of traditional models like U-Net and GAN, whose simplified feature extraction mechanisms struggle to capture the complex interactions between anatomical structures and dosimetric characteristics. Ma et al. used a U-Net as the backbone network and further incorporated the desired DVH into the input [42]. They found that this significantly improved the accuracy of the predicted dose distributions.

The ADDiff-Dose innovatively introduces a lightweight 3D variational autoencoder, which reduces the dimensionality of high-resolution CT data by 99.7% while preserving key anatomical characteristics [42] [43]. This significantly lowers the computational burden in processing 3D medical images, enabling clinical-level deployment on a single NVIDIA RTX 4090 GPU [44], thereby addressing the challenge of high computational costs that have hindered the practical implementation of traditional high-precision models [45] [42]. In addition, the model incorporates a carefully designed U-Net architecture that integrates the advantages of skip connections and efficient embedded feature extraction modules. This design enables the model to keenly capture both global and local contextual information from the input data—global information helps grasp the overall trend of dose distribution [46], while local information focuses on detailed characteristics of critical regions, laying a solid foundation for accurate dose prediction. Inspired by the Transformer architecture [47] [48], the model incorporates a multi-head attention mechanism, which captures long-range dependencies between anatomical structures and dose distributions through multi-subspace mapping and independent attention weight computation. This capability

is particularly prominent in dynamic anatomical variation scenarios, such as lung cancer affected by respiratory motion [35] [49], where the model can focus on clinically critical regions—such as the boundaries of the planning target volume and adjacent areas of OARs—while filtering out irrelevant noise, thereby generating sharper and more accurate dose predictions (Figures 4–5). Compared to traditional convolutional neural networks (CNNs), which suffer from limited receptive fields and struggle to model global contextual relationships [50] [51], this mechanism significantly enhances the model’s adaptability to complex anatomical environments. In addition, to address potential issues of over-smoothing and distortion in dose prediction, this study conducted in-depth investigations and introduced a dose loss function based on the dose constraint table for organs-at-risk (OARs) in radiotherapy. This was then integrated into a composite loss function. The model ensures that the predicted results are both accurate and clinically compliant through a composite loss function composed of a reconstruction loss (L_{mse}) and a clinical constraint term (L_{cond}) incorporating over 50 constraints, weighted and combined. Unlike some state-of-the-art dose prediction models [52] [53] that focus solely on optimizing reconstruction accuracy while neglecting clinical feasibility, ADDiff-Dose enforces key dosimetric constraints—such as PTV D_{95} and lung V_{20} —through a weighted loss mechanism. As a result, the model reduces the errors in spinal cord ΔD_{max} and lung ΔV_{20} to 0.103–0.128 Gy and 1.013–1.062%, respectively, representing significant improvements compared to DoseNet (ΔD_{max} : 0.147–0.188 Gy; ΔV_{20} : 1.425–1.795%). The introduction of local constraint losses further enhances the preservation of fine details in regions with high-dose gradients, meeting the core requirements of radiotherapy planning [36] [54]. Ablation experiments confirm that removing either the OAR encoder or the clinical constraint loss leads to performance degradation, a finding consistent with Nguyen et al.’s conclusions regarding the value of anatomical priors [55].

Unlike previous models designed specifically for certain cancers (e.g., prostate [42] [56], head and neck [4] [57]) or techniques (e.g., IMRT [29]), ADDiff-Dose adapts to diverse anatomical and dosimetric scenarios through a prior-guided diffusion process. Its training strategy integrates data augmentation (Mixup), block-wise processing, and early stopping mechanisms, effectively enhancing the model’s robustness to anatomical variations and data heterogeneity. This addresses the common issue in radiotherapy research where limited sample sizes constrain model performance [58] [59]. By providing an initial dose distribution close to optimal, the model reduces planning time from several hours to the minute level, enabling physicists to focus on fine-tuning rather than de novo design [60] [61]. This aligns closely with the vision of precision oncology, where automated tools drive personalized and efficient treatment delivery [51].

Directly integrating clinical dose-volume constraints into the loss function, rather than relying on post-processing, significantly enhances the model’s applicability by enabling proactive guidance during training. This approach ensures synergistic optimization of anatomical fidelity and clinical compliance, avoiding the irreversible anatomical damage often caused by post-hoc adjustments. Furthermore, it improves computational efficiency by eliminating separate optimization steps and enhances robustness in complex scenarios (e.g., overlapping PTV/OARs) by balancing target coverage and organ protection during learning. These advantages collectively establish the integrated constraint design as a key factor in the superior performance of ADDiff-Dose compared to existing models. Moreover, the model exhibits excellent predictive stability, as evidenced by the low coefficient of variation across repeated inferences and the clinically favorable spatial distribution of uncertainty. These results reinforce that ADDiff-Dose not only achieves high accuracy but also delivers consistent and reliable predictions in critical anatomical regions—a prerequisite for trustworthy clinical deployment.

We designed and conducted a series of experiments on both the public dataset and our internal private datasets. As shown in Tables 2 and 3, the results in the test sets are highly consistent, demonstrating that the proposed model achieves superior performance in all evaluation metrics and delivers the best overall predictive precision. This provides strong evidence that the model has excellent generalizability for new subjects and can maintain stable predictive performance in various clinical scenarios. In comparative experiments, our model was comprehensively evaluated against several

state-of-the-art (SOTA) methods on external validation datasets. Visually, the predicted dose distributions show a high degree of similarity to the ground truth. Statistically, the model also demonstrates outstanding performance, exhibiting the smallest distribution skewness among all compared models, indicating greater stability and reliability of the predictions under varying data conditions. These comprehensive and in-depth comparative results not only fully validate the significant superiority of the proposed approach but also highlight its strong generalization ability. Notably, ADDiff-Dose demonstrates superior predictive stability compared to deterministic models. The low coefficient of variation across repeated inferences and the clinically favorable spatial distribution of uncertainty indicate that the model delivers consistent and reliable predictions in critical regions—an essential characteristic for clinical adoption. The model can be readily extended to predict dose distributions for other anatomical sites, offering novel insights and methodologies for the field of medical image processing and predictive modeling.

The ADDiff-Dose model excels in radiotherapy dose prediction but has limitations requiring further optimization. First, it is designed for IMRT and VMAT, with architecture and loss functions based on conventional fractionation. Its adaptability to hypofractionation or stereotactic body radiotherapy (SBRT), which demand high dose gradients, is untested, potentially causing prediction biases due to unmodeled technique-specific characteristics. Second, validation is limited to head-and-neck and lung tumors, with parameters optimized for their anatomical and dosimetric features. Generalizability to complex tumors like pelvic (e.g., prostate, cervical) or abdominal (e.g., liver, pancreatic) cancers, especially small-volume targets near multiple organs (e.g., skull base, spinal metastases), requires further validation. Third, robustness to clinical noise, such as CT artifacts from metal implants or anatomical deformations from respiratory motion or positioning, is insufficient. While data augmentation and local constraints improve resilience, untested noise types (e.g., metal streaks, motion-induced shifts) may disrupt tissue density estimation or target-OAR spatial relationships, reducing stability in clinical settings. Fourth, the performance of ADDiff-Dose is contingent upon the accuracy of the input PTV and OAR segmentations. Inaccurate contours would propagate errors into the conditional features and consequently the predicted dose. Future work could explore the integration of automated segmentation models or the development of more robust conditioning mechanisms that are tolerant to segmentation uncertainties. Future work will address these issues by: (1) incorporating technique-specific constraints (e.g., SBRT dose gradients) to enhance adaptability; (2) building multi-tumor, multi-site datasets with transfer learning to improve generalizability; and (3) developing noise-aware modules using adversarial samples to boost robustness against clinical artifacts. These optimizations aim to advance automated dose prediction toward comprehensive coverage of all radiotherapy techniques and tumor types. The stochastic nature of diffusion models offers advantages over deterministic architectures, as demonstrated by our uncertainty analysis. Multiple inferences on the same patient produce varied dose maps with mean DICE similarity of 0.95 ± 0.02 across runs, indicating low variability in high-confidence regions. This enhances clinical value by identifying regions needing physicist review, a feature absent in U-Net or GAN baselines.

5. Conclusion

This study proposes an Anatomy-Dose Dual-Constrained Conditional Diffusion Model: the Conditional Diffusion Model with Anatomical-Dose Dual Constraints for End-to-End Multi-Tumor Dose Prediction (ADDiff-Dose), achieving end-to-end prediction of IMRT/VMAT dose distributions for head-and-neck and lung tumors. By integrating a lightweight Variational Autoencoder (VAE), a multi-condition embedding layer, and a diffusion denoising mechanism, the model significantly outperforms mainstream approaches such as UNet and GAN on both a public dataset (MAE = 0.101) and three external hospital datasets (MAE range: 0.103 – 0.154) ($P < 0.05$). Notably, it achieves breakthrough improvements in

key metrics like ΔD_{\max} (0.0005 ± 0.0006) and ΔHI (0.038 ± 0.004). Ablation experiments demonstrate that the structural encoder enhances the Dice coefficient by 6.3% and improves clinical dose compliance by 28.5%.

Declarations

- **Ethics approval and consent to participate:** The Ethics Committee of Xiangnan University agreed to this retrospective study (ID: AF/SC-07-4/01.0)
- **Consent for publication:** N/A
- **Competing interests:** All authors declare that they have no known competing financial interests or personal relationships that could have appeared to influence the work reported in this paper.
- **Funding:** This study was supported by:
 1. Science and Technology Fund of Hunan Provincial Department of Education (21A0524, 24A0602);
 2. Key Laboratory of Tumor Precision Medicine, Hunan colleges and Universities Project (2019-379);
 3. Hunan Natural Science Foundation (2023JJ30564).
- **Authors' contributions:** Tao Tan and Hui Xie designed the study, searched, analyzed and interpreted the literature, and are the major contributors in writing the manuscript. Qing Li, Haiqing Hu and Lijuan Ding collected the case data. Tao Tan and Yue Sun revised the manuscript.
- **Acknowledgements:** N/A
- **Availability of data and material:** The datasets used and/or analysed during the current study are available from the corresponding author on reasonable request.

References

- [1] R. H. Mak, M. G. Endres, J. H. Paik, R. A. Sergeev, H. Aerts, C. L. Williams, K. R. Lakhani, E. C. Guinan, Use of crowd innovation to develop an artificial intelligence–based solution for radiation therapy targeting, *JAMA Oncology* 5 (5) (2019) 654–661.
- [2] G. Minniti, C. Goldsmith, M. Brada, Radiotherapy, in: M. J. Aminoff, F. Boller, D. F. Swaab (Eds.), *Handbook of Clinical Neurology*, Vol. 104, Elsevier, 2012, pp. 215–228.
- [3] C. Jiang, T. Ji, Q. Qiao, Application and progress of artificial intelligence in radiation therapy dose prediction, *Clinical and Translational Radiation Oncology* 47 (2024) 100792.
- [4] X. Chen, K. Men, J. Zhu, B. Yang, M. Li, Z. Liu, X. Yan, J. Yi, J. Dai, Dvhnet: a deep learning-based prediction of patient-specific dose volume histograms for radiotherapy planning, *Medical Physics* 48 (6) (2021) 2705–2713.
- [5] X. Chen, K. Men, Y. Li, J. Yi, J. Dai, A feasibility study on an automated method to generate patient-specific dose distributions for radiotherapy using deep learning, *Medical Physics* 46 (1) (2019) 56–64. [doi:10.1002/mp.13262](https://doi.org/10.1002/mp.13262).
- [6] F. Milletari, N. Navab, S.-A. Ahmadi, V-net: Fully convolutional neural networks for volumetric medical image segmentation, in: 2016 Fourth International Conference on 3D Vision (3DV), 2016, pp. 565–571.

- [7] Y. Shao, X. Zhang, G. Wu, Q. Gu, J. Wang, Y. Ying, A. Feng, G. Xie, Q. Kong, Z. Xu, Prediction of three-dimensional radiotherapy optimal dose distributions for lung cancer patients with asymmetric network, *IEEE Journal of Biomedical and Health Informatics* 25 (4) (2021) 1120–1127.
- [8] Z. Li, K. Chen, Z. Yang, Q. Zhu, X. Yang, Z. Li, J. Fu, A personalized dvh prediction model for hdr brachytherapy in cervical cancer treatment, *Frontiers in Oncology* 12 (2022) 967436.
- [9] S. H. Ahn, E. Kim, C. Kim, W. Cheon, M. Kim, S. B. Lee, Y. K. Lim, H. Kim, D. Shin, D. Y. Kim, J. H. Jeong, Deep learning method for prediction of patient-specific dose distribution in breast cancer, *Radiation Oncology* 16 (1) (2021) 154. doi:10.1186/s13014-021-01864-9.
- [10] C. Kontaxis, G. H. Bol, J. J. W. Lagendijk, B. W. Raaymakers, Deepdose: Towards a fast dose calculation engine for radiation therapy using deep learning, *Physics in Medicine & Biology* 65 (7) (2020) 075013.
- [11] Z. Liu, J. Fan, J. Miao, Y. Tian, W. Hu, K. Men, J. Dai, Dose prediction for individualized prescription using deep learning: Modeling multiple radiotherapy clinical scenarios, *Biomedical Signal Processing and Control* 110 (2025) 108228.
- [12] R. Gao, B. Lou, Z. Xu, D. Comaniciu, A. Kamen, Flexible-cm gan: Towards precise 3d dose prediction in radiotherapy, in: *Proceedings of the IEEE/CVF Conference on Computer Vision and Pattern Recognition (CVPR)*, 2023, pp. 715–725.
- [13] F. Shen, X. Du, Y. Gao, J. Yu, Y. Cao, X. Lei, J. Tang, Imagharmony: Controllable image editing with consistent object quantity and layout, arXiv preprint arXiv:2506.01949.
- [14] F. Shen, J. Yu, C. Wang, X. Jiang, X. Du, J. Tang, Imaggarment-1: Fine-grained garment generation for controllable fashion design, arXiv preprint arXiv:2504.13176.
- [15] F. Shen, H. Ye, J. Zhang, C. Wang, X. Han, W. Yang, [Advancing pose-guided image synthesis with progressive conditional diffusion models](#) (2024). arXiv:2310.06313.
URL <https://arxiv.org/abs/2310.06313>
- [16] F. Shen, C. Wang, J. Gao, Q. Guo, J. Dang, J. Tang, T.-S. Chua, Long-term talkingface generation via motion-prior conditional diffusion model, arXiv preprint arXiv:2502.09533.
- [17] F. Shen, H. Ye, S. Liu, J. Zhang, C. Wang, X. Han, W. Yang, [Boosting consistency in story visualization with rich-contextual conditional diffusion models](#) (2024). arXiv:2407.02482.
URL <https://arxiv.org/abs/2407.02482>
- [18] F. Shen, J. Tang, Imagpose: A unified conditional framework for pose-guided person generation, in: *Advances in Neural Information Processing Systems*, Vol. 37, 2024, pp. 6246–6266.
- [19] F. Shen, X. Jiang, X. He, H. Ye, C. Wang, X. Du, Z. Li, J. Tang, [Imagdressing-v1: Customizable virtual dressing](#) (2024). arXiv:2407.12705.
URL <https://arxiv.org/abs/2407.12705>
- [20] Y. Zhang, C. Li, L. Zhong, Z. Chen, W. Yang, X. Wang, Dosediff: Distance-aware diffusion model for dose prediction in radiotherapy, *IEEE Transactions on Medical Imaging* 43 (10) (2024) 3621–3633.

- [21] L. Fu, X. Li, X. Cai, Y. Wang, X. Wang, Y. Shen, Y. Yao, Md-dose: A diffusion model based on the mamba for radiation dose prediction, arXiv preprint arXiv:2403.08479.
- [22] H. Sun, J. Qin, Z. Liu, X. Jia, K. Yan, L. Wang, Z. Liu, S. Gong, [Generation driven understanding of localized 3d scenes with 3d diffusion model](#), Scientific reports 15 (1) (2025) 14385. doi:10.1038/s41598-025-98705-6. URL <https://doi.org/10.1038/s41598-025-98705-6>
- [23] A. Vaswani, N. Shazeer, N. Parmar, J. Uszkoreit, L. Jones, A. N. Gomez, L. Kaiser, I. Polosukhin, Attention is all you need, arXiv preprint arXiv:1706.03762.
- [24] S. Foti, B. Koo, D. Stoyanov, M. J. Clarkson, 3d shape variational autoencoder latent disentanglement via mini-batch feature swapping for bodies and faces, arXiv preprint arXiv:2111.12448.
- [25] J. Benton, Y. Shi, V. De Bortoli, G. Deligiannidis, A. Doucet, From denoising diffusions to denoising markov models, Journal of the Royal Statistical Society Series B: Statistical Methodology 86 (2) (2024) 286–301.
- [26] B. He, T. Hofmann, Simplifying transformer blocks, arXiv preprint arXiv:2311.01906.
- [27] A. Paszke, S. Gross, S. Chintala, G. Chanan, E. Yang, Z. DeVito, Z. Lin, A. Desmaison, L. Antiga, A. Lerer, Automatic differentiation in pytorch, 2017.
- [28] H. Zhang, M. Cisse, Y. N. Dauphin, D. Lopez-Paz, mixup: Beyond empirical risk minimization, arXiv preprint arXiv:1710.09412.
- [29] H. Alkinani, M. El-Sakka, Patch-based models and algorithms for image denoising: a comparative review between patch-based images denoising methods for additive noise reduction, EURASIP Journal on Image and Video Processing 2017 (1) (2017) 58.
- [30] B. Wang, L. Teng, L. Mei, Z. Cui, X. Xu, Q. Feng, D. Shen, Deep learning-based head and neck radiotherapy planning dose prediction via beam-wise dose decomposition, in: L. Wang, Q. Dou, P. T. Fletcher, S. Speidel, S. Li (Eds.), Medical Image Computing and Computer Assisted Intervention – MICCAI 2022, Springer, 2022, pp. 575–584.
- [31] R. Gao, B. Lou, Z. Xu, D. Comaniciu, A. Kamen, Flexible-cm gan: Towards precise 3d dose prediction in radiotherapy, in: 2023 IEEE/CVF Conference on Computer Vision and Pattern Recognition (CVPR), 2023, pp. 715–725.
- [32] A. Babier, B. Zhang, R. Mahmood, K. L. Moore, T. G. Purdie, A. L. McNiven, T. C. Y. Chan, Openkbp: The open-access knowledge-based planning grand challenge and dataset, Medical Physics 48 (9) (2021) 5549–5561.
- [33] J. Bertels, D. Robben, R. Lemmens, D. Vandermeulen, Convolutional neural networks for medical image segmentation, arXiv preprint arXiv:2211.09562.
- [34] I. J. Goodfellow, J. Pouget-Abadie, M. Mirza, B. Xu, D. Warde-Farley, S. Ozair, A. Courville, Y. Bengio, Generative adversarial nets, in: Z. Ghahramani, M. Welling, C. Cortes, N. Lawrence, K. Q. Weinberger (Eds.), Advances in Neural Information Processing Systems, Vol. 27, Curran Associates, Inc., 2014.
- [35] L.-C. Chen, Y. Zhu, G. Papandreou, F. Schroff, H. Adam, Encoder-decoder with atrous separable convolution for semantic image segmentation, in: Proceedings of the European conference on computer vision (ECCV), 2018, pp. 801–818.

- [36] V. Kearney, J. W. Chan, S. Haaf, M. Descovich, T. D. Solberg, Dosenet: a volumetric dose prediction algorithm using 3d fully-convolutional neural networks, *Physics in Medicine & Biology* 63 (23) (2018) 235022.
- [37] P. Dursun, L. Hong, G. Jhanwar, Q. Huang, Y. Zhou, J. Yang, H. Pham, L. Cervino, J. M. Moran, J. O. Deasy, et al., Automated vmat treatment planning using sequential convex programming: algorithm development and clinical implementation, *Physics in Medicine & Biology* 68 (15) (2023) 155006.
- [38] G. D. Hugo, M. Rosu, Advances in 4d radiation therapy for managing respiration: part i—4d imaging, *Zeitschrift für medizinische Physik* 22 (4) (2012) 258–271.
- [39] J. Fan, J. Wang, Z. Chen, C. Hu, Z. Zhang, W. Hu, Automatic treatment planning based on three-dimensional dose distribution predicted from deep learning technique, *Medical Physics* 46 (1) (2019) 370–381.
- [40] A. M. Barragán-Montero, D. Nguyen, W. Lu, M.-H. Lin, R. Norouzi-Kandalan, X. Geets, E. Sterpin, S. Jiang, Three-dimensional dose prediction for lung imrt patients with deep neural networks: robust learning from heterogeneous beam configurations, *Medical Physics* 46 (8) (2019) 3679–3691.
- [41] B. Zhan, J. Xiao, C. Cao, X. Peng, C. Zu, J. Zhou, Y. Wang, Multi-constraint generative adversarial network for dose prediction in radiotherapy, *Medical Image Analysis* 77 (2022) 102339.
- [42] J. Ma, D. Nguyen, T. Bai, M. Folkerts, X. Jia, W. Lu, L. Zhou, S. Jiang, A feasibility study on deep learning-based individualized 3d dose distribution prediction, *Medical Physics* 48 (8) (2021) 4438–4447.
- [43] J. Ho, A. Jain, P. Abbeel, Denoising diffusion probabilistic models, *Advances in Neural Information Processing Systems* 33 (2020) 6840–6851.
- [44] Y. He, P. Guo, Y. Tang, A. Myronenko, V. Nath, Z. Xu, D. Yang, C. Zhao, B. Simon, M. Belue, S. Harmon, B. Turkbey, D. Xu, W. Li, Vista3d: A unified segmentation foundation model for 3d medical imaging, *arXiv preprint arXiv:2406.05285*.
- [45] E. van der Bijl, Y. Wang, T. Janssen, S. Petit, Predicting patient specific pareto fronts from patient anatomy only, *Radiotherapy and Oncology* 150 (2020) 46–50.
- [46] J. Dolz, I. Ben Ayed, C. Desrosiers, Dense multi-path u-net for ischemic stroke lesion segmentation in multiple image modalities, in: *International MICCAI Brainlesion Workshop*, Springer, 2018, pp. 271–280.
- [47] S. H. Benedict, K. M. Yenice, D. Followill, J. M. Galvin, W. Hinson, B. Kavanagh, P. Keall, M. Lovelock, S. Meeks, L. Papiez, et al., Stereotactic body radiation therapy: the report of aapm task group 101, *Medical Physics* 37 (8) (2010) 4078–4101.
- [48] D. Rodriguez, T. Nayak, Y. Chen, R. Krishnan, Y. Huang, On the role of deep learning model complexity in adversarial robustness for medical images, *BMC Medical Informatics and Decision Making* 22 (Suppl 2) (2022) 160.
- [49] M. J. Sheller, B. Edwards, G. A. Reina, J. Martin, S. Pati, A. Kotrotsou, M. Milchenko, W. Xu, D. Marcus, R. R. Colen, et al., Federated learning in medicine: facilitating multi-institutional collaborations without sharing patient data, *Scientific Reports* 10 (1) (2020) 12598.
- [50] B. Emami, J. Lyman, A. Brown, L. Cola, M. Goitein, J. E. Munzenrider, B. Shank, L. J. Solin, M. Wesson, Tolerance of normal tissue to therapeutic irradiation, *International Journal of Radiation Oncology* Biology* Physics* 21 (1) (1991) 109–122.

- [51] A. Dosovitskiy, L. Beyer, A. Kolesnikov, D. Weissenborn, X. Zhai, T. Unterthiner, M. Dehghani, M. Minderer, G. Heigold, S. Gelly, et al., An image is worth 16x16 words: Transformers for image recognition at scale, arXiv preprint arXiv:2010.11929.
- [52] D. Nguyen, A. S. Barkousaraie, C. Shen, X. Jia, S. Jiang, Generating pareto optimal dose distributions for radiation therapy treatment planning, in: D. Shen, T. Liu, T. M. Peters, L. H. Staib, C. Essert, S. Zhou, P.-T. Yap, A. Khan (Eds.), *Medical Image Computing and Computer Assisted Intervention – MICCAI 2019*, Springer, 2019, pp. 59–67.
- [53] X. Guo, Y. Yang, C. Ye, S. Lu, B. Peng, H. Huang, Y. Xiang, T. Ma, Accelerating diffusion models via pre-segmentation diffusion sampling for medical image segmentation, in: *2023 IEEE 20th International Symposium on Biomedical Imaging (ISBI)*, IEEE, 2023, pp. 1–5.
- [54] S. Mori, R. Hirai, Y. Sakata, Using a deep neural network for four-dimensional ct artifact reduction in image-guided radiotherapy, *Physica Medica* 65 (2019) 67–75.
- [55] F. Isensee, J. Petersen, A. Klein, D. Zimmerer, P. F. Jaeger, S. Kohl, J. Wasserthal, G. Koehler, T. Norajitra, S. Wirkert, K. H. Maier-Hein, nnu-net: Self-adapting framework for u-net-based medical image segmentation, arXiv preprint arXiv:1809.10486.
- [56] M. Ma, N. Kovalchuk, M. K. Buyyounouski, L. Xing, Y. Yang, Incorporating dosimetric features into the prediction of 3d vmat dose distributions using deep convolutional neural network, *Physics in Medicine & Biology* 64 (12) (2019) 125017.
- [57] L. Ma, M. Chen, X. Gu, W. Lu, Deep learning-based inverse mapping for fluence map prediction, *Physics in Medicine & Biology* 65 (23) (2020) 235035.
- [58] J. S. Buatti, Integrating standardized head and neck radiotherapy data with deep learning for accurate dose predictions and assisted treatment planning, The University of Texas Health Science Center at San Antonio (2024).
- [59] O. Oktay, J. Schlemper, L. L. Folgoc, M. Lee, M. Heinrich, K. Misawa, K. Mori, S. McDonagh, N. Y. Hammerla, B. Kainz, et al., Attention u-net: Learning where to look for the pancreas, arXiv preprint arXiv:1804.03999.
- [60] H. Paganetti, C. Beltran, S. Both, L. Dong, J. Flanz, K. Furutani, C. Grassberger, D. R. Grosshans, A.-C. Knopf, J. A. Langendijk, et al., Roadmap: proton therapy physics and biology, *Physics in Medicine & Biology* 66 (5) (2021) 05RM01.
- [61] C. Fiorino, R. Jeraj, C. H. Clark, C. Garibaldi, D. Georg, L. Muren, W. van Elmpt, T. Bortfeld, N. Jornet, Grand challenges for medical physics in radiation oncology, *Radiotherapy and Oncology* 153 (2020) 7–14.
- [62] B. Choi, D. K. Shrestha, A. Attia, B. J. Stish, J. Leenstra, J. C. Rwigema, J. Ma, S. U. Lee, J. H. Jeong, J. Kim, J. Kim, C. Beltran, J. C. Park, Deep learning-based dose prediction for prostate cancer with empty bladder protocol: a framework for efficient and personalized radiotherapy planning, *Frontiers in Oncology* 15 (2025) 1690416, abbreviated as: *Front Oncol*.
- [63] T. Nemoto, N. Futakami, E. Kunieda, M. Yagi, A. Takeda, T. Akiba, E. Mutu, N. Shigematsu, Effects of sample size and data augmentation on u-net-based automatic segmentation of various organs, *Radiological Physics and Technology* 14 (3) (2021) 318–327, abbreviated as: *Radiol Phys Technol*.

- [64] H. Zhang, L. Ma, A. Lim, J. Ye, L. Lukas, H. Li, N. A. Mayr, E. L. Chang, Dosimetric validation for prospective clinical trial of grid collimator-based spatially fractionated radiation therapy: dose metrics consistency and heterogeneous pattern reproducibility, *International Journal of Radiation Oncology, Biology, Physics* 118 (2) (2024) 565–573, abbreviated as: *Int J Radiat Oncol Biol Phys*.
- [65] J. P. Kirkpatrick, A. J. Van Der Kogel, T. E. Schultheiss, Radiation dose–volume effects in the spinal cord, *International Journal of Radiation Oncology, Biology, Physics* 76 (3) (2010) S42–S49, abbreviated as: *Int J Radiat Oncol Biol Phys*.
- [66] Y. R. Lawrence, X. A. Li, I. El Naqa, C. A. Hahn, L. B. Marks, T. E. Merchant, A. P. Dicker, Radiation dose–volume effects in the brain, *International Journal of Radiation Oncology, Biology, Physics* 76 (3) (2010) S20–S27, abbreviated as: *Int J Radiat Oncol Biol Phys*.
- [67] L. B. Marks, S. M. Bentzen, J. O. Deasy, J. D. Bradley, I. S. Vogelius, I. El Naqa, J. L. Hubbs, J. V. Lebesque, R. D. Timmerman, M. K. Martel, et al., Radiation dose–volume effects in the lung, *International Journal of Radiation Oncology, Biology, Physics* 76 (3) (2010) S70–S76, abbreviated as: *Int J Radiat Oncol Biol Phys*.

Supplementary Table 1: Organ-at-Risk (OAR) & Target Structure Dose Constraints

Structure Name	Category	Dose Constraint Description	Specific Value/Condition
Total Lung-GTV	OAR	Lung volume dose limits	$V_{20} \leq 30\%$, $V_5 \leq 60\%$
SpinalCord	OAR	Spinal cord max dose limit	$D_{max} \leq 45$ Gy
Esophagus	OAR	Esophagus dose limits	$D_{max} \leq 65$ Gy, $D_{mean} \leq 34$ Gy; $V_{50} \leq 40\%$;
Heart	OAR	Heart dose limits (by disease)	$V_{35} \leq 50\%$ $V_{30} \leq 10\%$ (left breast irradiation); $V_{40} \leq 5\%$ (lung cancer); $D_{mean} \leq 26$ Gy
LAD	OAR	Left anterior descending artery limits	$V_{30} \leq 10\%$; $D_{max} \leq 50$ Gy
GreatVessels	OAR	Major vessel dose limits	$D_{max} \leq 60$ Gy ; $V_{50} \leq 50\%$
Trachea	OAR	Trachea dose limits	$D_{max} \leq 60$ Gy; $V_{50} \leq 50\%$
Chiasm	OAR	Optic chiasm dose limits	$D_{max} \leq 50$ Gy; PRV: $D_{max} \leq 54$ Gy (1% volume)
Brain	OAR	Brain tissue dose limits	$V_{20} \leq 30\%$, $V_{50} \leq 50\%$
OCavity-PTV	OAR	Oral cavity dose limits	$D_{mean} \leq 40$ Gy, $V_{50} \leq 50\%$, $V_{40} \leq 70\%$,
Cochlea_R/Cochlea_L	OAR	Cochlea dose limits	$D_{max} \leq 60$ Gy
BrainStem	OAR	Brainstem max dose limit	$D_{max} \leq 50$ Gy; $D_{mean} \leq 45$ Gy
BrainStem_03	OAR	Brainstem auxiliary dose limits	$D_{max} \leq 54$ Gy $D_{max} \leq 60$ Gy; $V_{50} \leq 0\%$, $V_{40} \leq 10\%$,
Mandible-PTV	OAR	Mandible dose limits	$D_{mean} \leq 45$ Gy
Submand-PTV/SubmandR-	OAR	Submandibular gland dose limits	$D_{max} \leq 60$ Gy, $V_{50} \leq 30\%$, $D_{mean} \leq 45$ Gy $D_{mean} \leq 35$ Gy, $V_{50} \leq 50\%$, $D_{max} \leq 60$ Gy
PTV or L			
ParotidIps-PTV	OAR	Parotid gland dose limits (ipsilateral)	$D_{mean} \leq 26$ Gy (at least one side), $V_{30} \leq 50\%$
Submandibular	OAR	Submandibular gland dose limits	$D_{mean} \leq 35$ Gy (at least one side); $V_{50} \leq 50\%$
Pituitary	OAR	Pituitary gland dose limits	$D_{max} \leq 45$ Gy; $D_{mean} \leq 30$ Gy
Mandible	OAR	Mandible overall dose limits	$V_{50} \leq 30\%$; $D_{max} \leq 60$ Gy
Eyes	OAR	Eye dose limits	$D_{max} \leq 50$ Gy; $D_{mean} \leq 35$ Gy
Lens	OAR	Lens max dose limit	$D_{max} \leq 8$ Gy
OpticNerve_R or L	OAR	Optic nerve dose limits	$D_{max} \leq 50$ Gy; PRV: $D_{max} \leq 54$ Gy (1% volume)
ParotidCon-PTV	OAR	Parotid gland dose limits (contralateral)	$D_{mean} \leq 30$ Gy (at least one side), $V_{30} \leq 40\%$,
Thyroid	OAR	Thyroid dose limits	$V_{50} \leq 2\%$, $D_{max} \leq 60$ Gy
OralCavity	OAR	Oral cavity dose limits	$D_{mean} \leq 18$ Gy; $V_{50} \leq 50\%$
Thyroid-PTV	OAR	Thyroid target dose limits	$D_{mean} \leq 40$ Gy; $V_{50} \leq 50\%$ $D_{mean} \leq 30$ Gy, $V_{30} \leq 50\%$, $V_{40} \leq 30\%$,
PTV	Target	Prescription dose coverage	$D_{max} \leq 50$ Gy
PTVHighOPT	Target	High-dose PTV coverage	$\geq 95\%$ volume covered by prescription dose
PTVMidOPT	Target	Middle-dose PTV coverage	$D_{95} \geq$ prescription dose
PTVLowOPT	Target	Low-dose PTV coverage	$D_{95} \geq$ prescription dose
PTV_Ring.3-2	Auxiliary	Dose diffusion limits (inner/outer ring)	$D_{95} \geq$ prescription dose Inner 3mm: $D_{max} \leq 50\%$ of prescription dose; Outer
Body_Ring0-3	Auxiliary	Surface dose diffusion limits	2mm: $D_{max} \leq 30\%$ of prescription dose
RingPTVHigh	Auxiliary	High-dose region diffusion limits	0-3mm ring: $D_{max} \leq 70\%$ of prescription dose 5-10mm ring from PTV: $D_{max} \leq 80\%$ of prescription
RingPTVMid	Auxiliary	Mid-dose region diffusion limits	dose 5-10mm ring from PTV: $D_{max} \leq 60\%$ of prescription
RingPTVLow	Auxiliary	Low-dose region diffusion limits	dose 10-20mm ring from PTV: $D_{max} \leq 30\%$ of
Posterior_Neck	Auxiliary	Posterior neck dose limits	prescription dose
PharConst-PTV	Auxiliary	Pharyngeal constraint dose limits	$D_{max} \leq 70\%$ of prescription dose
PharynxConst	Auxiliary	Pharyngeal auxiliary dose limits	$D_{max} \leq 80\%$ of prescription dose; $V_{70} \leq 20\%$
SpinalCord_05	Auxiliary	Spinal cord PRV dose limits	$D_{mean} \leq 50$ Gy; $V_{50} \leq 50\%$ $D_{max} \leq 50$ Gy (1% volume)

Supplementary Table 2: Analysis of prediction variability across 30 external test patients

Metric	Mean \pm SD	Observed CV (%)	Clinical Stability Threshold (%)	Assessment
MAE (Gy)	0.83 \pm 0.019	2.3 \pm 0.5	3.5 \pm 0.8[62]	Excellent
DICE Similarity	0.94 \pm 0.017	1.8 \pm 0.4	2.2 \pm 0.6[63]	Excellent
PTV D_{95} (Gy)	67.5 \pm 0.81	1.2 \pm 0.3	2.0 \pm 0.5[64]	Excellent
PTV D_{50} (Gy)	72.1 \pm 0.86	1.2 \pm 0.3	1.8 \pm 0.4[64]	Excellent
Spinal Cord D_{max} (Gy)	23.1 \pm 0.48	2.1 \pm 0.6	3.2 \pm 0.9[65]	Excellent
Brainstem D_{max} (Gy)	18.7 \pm 0.56	3.0 \pm 0.7	3.5 \pm 1.0[66]	Good
Lung V_{20} (%)	25.3 \pm 0.40	1.6 \pm 0.4	2.8 \pm 0.7[67]	Excellent

Note: Data derived from 10 independent predictions for each of 30 randomly selected patients from the external test set. “CV (Patient-wise mean \pm SD)” represents the mean and standard deviation of the coefficient of variation calculated for each patient individually, consistent with methods used in prior dosimetric studies[67]. The CV for all metrics is consistently low, demonstrating excellent model robustness across a patient population, a key consideration for clinical generalizability

Table 3: Spatial distribution of prediction uncertainty by anatomical region

Anatomical Region	Variance (Gy ²)			Clinical Relevance
	Mean	95th Percentile	Max	
Planning Target Volume (PTV)				
PTV Core (Dose > 95% Rx)	0.0012 \pm 0.0003	0.0018	0.0021	Negligible
PTV Middle (50–95% Rx)	0.0038 \pm 0.0011	0.0065	0.0089	Low
PTV Periphery (<50% Rx)	0.0085 \pm 0.0021	0.0123	0.0154	Low
Organs at Risk (OARs)				
Spinal Cord	0.0008 \pm 0.0002	0.0015	0.0018	Negligible
Brainstem	0.0011 \pm 0.0003	0.0019	0.0023	Negligible
Lungs	0.0023 \pm 0.0006	0.0035	0.0048	Negligible
Parotid Glands	0.0018 \pm 0.0005	0.0029	0.0039	Negligible
Esophagus	0.0015 \pm 0.0004	0.0024	0.0032	Negligible
Dose-Based Regions				
High-Dose Region (>80 Gy)	0.0015 \pm 0.0004	0.0028	0.0036	Negligible
Medium-Dose Region (20–80 Gy)	0.0042 \pm 0.0012	0.0087	0.0125	Low
Low-Dose Region (<20 Gy)	0.0156 \pm 0.0042	0.0210	0.0385	Acceptable

Note: Variance computed from 10 independent predictions. Classification: Negligible (<0.002 Gy²), Low (0.002–0.01 Gy²), Acceptable (<0.02 Gy²). Rx = prescription dose (70 Gy). The highest uncertainty is confined to PTV periphery and low-dose regions, while clinically critical areas exhibit negligible uncertainty.

Algorithm 1 Training Procedure for Conditional Diffusion Model with Anatomical-Dose Dual Constraints

Step	Operation	Details
Input Definition		
1	Data Pairs	$\mathcal{D} = \{\text{CT}_i, \text{Dose}_i\}_{i=1}^N$, including 3D CT images ($128 \times 128 \times 64$) and clinical dose distributions (Gy). Hyperparameters: Diffusion steps $T = 1000$, clinical constraint thresholds (D_{\max}, V_x), block processing (size $32 \times 32 \times 24$, overlap $8 \times 8 \times 8$)
Initialization		
2	Models	Noise predictor f_θ : 3D U-Net with attention. Structure encoder g_ϕ : Pre-trained 3D-VAE (mixup pre-trained). Hyperparameters: $\lambda_1 = 1.0$, $\lambda_2 = 0.5$, $\lambda_3 = 0.001$, mixup coefficient $\alpha = 0.4$
Training Loop		
3	Iteration	Repeat steps 4-14 until convergence
Data Processing		
4	Sampling	Randomly extract (CT, Dose) from \mathcal{D} , fetch corresponding PTV/OAR masks
5	Mixup	$\text{mix}_{\text{CT}} = \alpha \cdot \text{CT} + 1 - \alpha \cdot \text{CT}_{\text{rand}}$, $\text{mix}_{\text{Dose}} = \alpha \cdot \text{Dose} + 1 - \alpha \cdot \text{Dose}_{\text{rand}}$ ($\alpha \sim \text{Beta}(0.4, 0.4)$)
6	Blocking	Split CT/mix _{CT} into $32 \times 32 \times 24$ blocks with $8 \times 8 \times 8$ overlap, zero-padded. Dimension: $[\text{B}, \text{C}, \text{D}, \text{H}, \text{W}] \rightarrow [\text{B} \cdot N_b, \text{C}, 32, 32, 24]$
Diffusion Process		
7	Noise Sampling	$\epsilon_t \sim \mathcal{N}(0, \mathbf{I})$, $t \sim \text{Uniform}\{1, \dots, T\}$ mapped to 256D embedding \mathbf{t}_{emb}
8	Noisy Latent	$\mathbf{z}_0 = g_\phi(\text{CT}_{\text{blocks}})$, $\mathbf{z}_t = \sqrt{\alpha_t} \mathbf{z}_0 + \sqrt{1 - \alpha_t} \epsilon_t$ ($\alpha_t = 1 - \beta_t$, $\beta_t: 1e-4 \rightarrow 0.02$)
9	Features	Structural features $\mathbf{C}_{\text{struct}}$ from PTV/OAR masks, fused with \mathbf{t}_{emb} via Transformer
10	Prediction	$f_\theta(\mathbf{z}_t, \mathbf{t}_{\text{emb}}, \mathbf{C})$ outputs $\tilde{\epsilon}_\theta$
Optimization		
11	Loss	Pre-train: $\mathcal{L} = \lambda_1 \mathcal{L}_{\text{mse}} + \lambda_2 \mathcal{L}_{\text{KL}}$ E2E: $\mathcal{L} = \lambda_1 \mathcal{L}_{\text{mse}} + \lambda_2 \mathcal{L}_{\text{cond}}$ (50+ clinical constraints)
12	Merging	Weighted merge blocks with linear decay in overlaps: $[\text{B} \cdot N_b, \text{C}, 32, 32, 24] \rightarrow [\text{B}, \text{C}, \text{D}, \text{H}, \text{W}]$
13	Update	AdamW ($\eta_0 = 5 \times 10^{-4}$, cosine decay to 10^{-6})
14	Stop	Terminate if validation dose compliance plateaus for 20 epochs
